Low-frequency Broadband Noise Absorption of Multi-chamber Micro-perforated Pane Absorbers in Normal and Grazing Acoustic Incidence

Jiayu Wang, Gareth Bennett, Thomas Humbert, Yves Aurégan, Mats Åbom, Hans Boden

Low-frequency Broadband Noise Absorption of Multi-chamber Micro-perforated Panel Absorbers in Normal and Grazing Acoustic Incidence

Jiayu Wang* and Gareth J. Bennett †
Trinity College Dublin, the University of Dublin, Dublin, Ireland

Thomas Humbert‡ and Yves Aurégan§
Le Mans Université, Le Mans, France

Mats Åbom ¶ and Hans Bodén‖
KTH Royal Institute of Technology, Stockholm, Sweden

This paper presents a significant advancement in micro-perforated panel absorber technologies. Two distinct types of sub-wavelength multi-chamber micro-perforated panel absorbers (MC-MPPA) for low-frequency broadband noise absorption under both normal and grazing acoustic incidence conditions are developed. Micro-perforated panel absorbers (MPPAs) exhibit versatility, eco-friendliness, and a straightforward, robust construction, making them ideal acoustic solutions. A graph-theory-based two-point impedance method (TpIM) and the Cremer impedance method are used for system modeling, enabling the design of the MC-MPPA to be optimized for maximum sound absorption in a chosen frequency range for both normal and grazing acoustic incidence. This graph theory approach represents a breakthrough, as an equivalent circuit model approach could not be applied to such complex models. Under normal incidence conditions, the experimental overall absorption coefficient is measured to be 0.8273 for a 22 mm thick MC-MPPA in the frequency range of [660 2000] Hz, and 0.8284 for a 52 mm thick MC-MPPA in the frequency range of [400 2000] Hz. Under grazing incidence conditions, an optimized MC-MPPA with a mere 30 mm sub-chamber depth achieves a transmission loss of 66 dB at 1180 Hz. Additionally, a 50 mm sub-chamber depth yields a transmission loss greater than 10 dB over an 880 Hz wide frequency range: [820 1700] Hz. The developed MC-MPPA technologies hold great promise for various duct noise attenuation applications including aeroengine acoustic liners.

I. Nomenclature

L	=	MC-MPPA length
W	=	MC-MPPA width
D	=	MC-MPPA air cavity depth
$D_{\max}$	=	depth of MC-MPPA's deepest sub-chamber
τ	=	panel thickness
τ_t	=	thickness of the top MPP in the MC-MPPA
τ_i	=	thickness of the inside MPP in the MC-MPPA
d	=	perforation diameter
d_t	=	perforation diameter of the top MPP in the MC-MPPA
d_i	=	perforation diameter of the internal MPP in the MC-MPPA

*PhD Student, Department of Mechanical, Manufacturing and Biomedical Engineering, AIAA Student Member, wangj12@tcd.ie
†Associate Professor, Department of Mechanical, Manufacturing and Biomedical Engineering, AIAA Senior Member, gareth.bennett@tcd.ie
‡Research Engineer, LAUM - Laboratoire d'Acoustique de l'Université du Mans, thomas.humbert@univ-lemans.fr
§Prof., LAUM - Laboratoire d'Acoustique de l'Université du Mans, yves.auregan@univ-lemans.fr
¶Prof. Emeritus, Department of Mechanics, Marcus Wallenberg Laboratory for Sound and Vibration Research, matsabom@kth.se
‖Prof. Emeritus, Department of Mechanics, Marcus Wallenberg Laboratory for Sound and Vibration Research, hansbod@kth.se

φ	=	perforation porosity
φ_t	=	perforation porosity of the top MPP in the MC-MPPA
φ_i	=	perforation porosity of the internal MPP in the MC-MPPA
n	=	perforation number
n_t	=	perforation number of the top MPP in the MC-MPPA
n_i	=	perforation number of the internal MPP in the MC-MPPA
$Z_{\text{mpp, Comsol}}$	=	acoustic impedance of the MPP provided by COMSOL
$Z_{\text{mpp, Maa}}$	=	acoustic impedance of the MPP provided by Maa
Z_{ac}	=	acoustic impedance of the air cavity
z	=	specific acoustic impedance
i	=	imaginary unit
ρ_0	=	air density
c_0	=	sound speed in air
ω	=	angular frequency
f	=	frequency in Hertz
J_n	=	n^{th} order Bessel function
μ	=	dynamic viscosity of air
$\Lambda(\varphi)$	=	Fok function
a_n	=	n^{th} coefficient
$\mathbf{L}$	=	Laplace matrix
$\mathcal{N}$	=	number of nodes
y_{ij}	=	admittance between nodes i and j
Z_{ij}	=	acoustic impedance between nodes i and j
$\dagger$	=	hermitian conjugation
η_β	=	eigenvalues of $\mathbf{L}^\dagger\mathbf{L}$
ψ_β	=	eigenvectors of $\mathbf{L}^\dagger\mathbf{L}$
λ_β	=	eigenvalues of $\mathbf{L}$
R	=	reflection coefficient
α	=	normal incidence sound absorption coefficient
M	=	Mach number
A	=	mode amplitude
Ψ	=	mode shape
k	=	wavenumber
k_x	=	x-axis component of the wavenumber k
k_y	=	the y-axis component of the wavenumber k
H	=	height of the duct
He	=	Helmholtz number
$Z_{\text{cr}}\vert_M$	=	normalized Cremer impedance
TL	=	sound transmission loss
R	=	acoustic resistance of MPP
χ	=	acoustic reactance of MPP
F_δ	=	flow effect on the MPP reactance
β	=	flow effect on the MPP resistance
K	=	shear wavenumber
R_s	=	surface resistance
α'	=	edge-related coefficient
δ	=	mass end correction coefficient
Re	=	real component
Im	=	imaginary component

II. Introduction

SINCE the advent of aviation, aircraft noise has been a persistent challenge for airlines, aircraft manufacturers, and particularly for individuals residing in the proximity to airports [1–7]. This form of noise pollution, ranked as the

third largest contributor to transportation-related noise, is intrusive and has the potential to harm human health when individuals are exposed to it for prolonged periods of time [8]. Sustained exposure to aircraft noise has been associated with various adverse consequences, including sleep disruption, hearing loss, cardiovascular disease, and elevated stress levels [9]. These concerns have prompted increased attention to the development of noise reduction technologies, improved aircraft design, and the implementation of regulations aimed at minimizing the impact of aircraft noise on surrounding communities. Organizations such as the International Civil Aviation Organization (ICAO) and the Advisory Council for Aviation Research and Innovation in Europe (ACARE) have taken steps to address the problem of aircraft noise pollution [10]. In order to mitigate the negative impact of aircraft noise, these organizations have proposed a range of recommended technological and operational objectives with a long-term focus of 10 years or more. For example, initiatives such as "Vision 2020" and "Flightpath 2050" have been introduced to guide the aviation industry towards more sustainable and responsible practices. By working towards these goals, the aviation industry can reduce the impact of aircraft noise on local populations and promote a more sustainable and responsible approach to air transportation.

Aircraft and engine manufacturers have made remarkable technical advancements in the reduction of noise produced by aircraft during takeoff and landing since the introduction of first-generation turbojet and low bypass ratio turbofan aircraft in the 1960s. The success of these technological developments has been noteworthy, with a decrease of over 20 Effective Perceived Noise Decibels (EPNdB) per aircraft operation since the implementation of noise certification procedures [11]. These procedures are defined by regulatory bodies such as the US Federal Aviation Administration and the International Civil Aviation Organization (ICAO), which utilize Federal Air Regulation (FAR) Part 36 and Annex 16 to the Convention on International Civil Aviation, respectively, to establish certification processes. Much of the reduction stems directly or indirectly from changes in the engine ByPass Ratio (BPR) with additional improvements coming from incremental improvements in noise reduction technology distinct from BPR changes [11]. With the continued advancement of material science and manufacturing methods, the BPR of turbofan engines is expected to increase even further. However, this presents significant challenges for aeroacousticians who are responsible for designing noise-absorbing technologies. Firstly, increasing engine diameters means that the space available for noise reduction liners is decreasing. Secondly, the noise output from the fan is decreasing in frequency, but with significant broadband content at low frequencies. Consequently, the reduction of low-frequency broadband duct noise at a deep sub-wavelength scale poses a significant challenge that is difficult to address.

Considering the significant challenges associated with further noise reduction in the fields of aircraft and aero-engine development, the pursuit of suitable and efficient sound-absorbing structures or materials is of the utmost importance. Porous materials such as open-cell polyurethane and melamine foams are effective at attenuating broadband noise. However, their efficiency is reliant on their overall thickness, which often renders them impractical for many real-world applications at low frequencies. In contrast, a micro-perforated panel absorber (MPPA) is a straightforward and robust solution that efficiently absorbs low-frequency, broadband noise with a deeply sub-wavelength structure, making it increasingly popular compared to porous material-based solutions [12–18]. To expand the use of MPPAs in reducing aeroengine fan noise, it is essential to study the sound absorption performance of MPPAs in a grazing acoustic and flow conditions and develop an effective MPPA for absorbing low-frequency broadband noise within ducts.However, the sound absorption performance of MPPAs under grazing acoustic conditions has received limited attention from researchers thus far. Rice [19] conducted a theoretical analysis of the oscillatory fluid flow in the vicinity of a circular orifice under a steady grazing flow. The study revealed that orifice resistance increases in direct proportion to grazing flow velocity and that the orifice mass reactance end correction remains unaffected by grazing flow. Rogers and Hersh [20] developed a semi-theoretical model for predicting the acoustic resistance of square-edged orifices under grazing flow condition. Following a similar approach as demonstrated in Rogers and Hersh [20], Hersh et al. [21] developed a semi-theoretical model for predicting the acoustic impedance of Helmholtz resonators consisting of single and clustered orifices when considering the effect of the grazing flow. Åbom et al. [22–24] examined the impact of grazing flow on the impedance of MPPs. Furthermore, they successfully developed the analytical models for MPPs with circular and slit-shaped holes under the grazing flow conditions and subsequently validated the models through experiments. Zhang and Cheng [25] conducted research on micro-perforated panels (MPPs) under low-speed grazing flow conditions. They proposed a model to predict the acoustic impedance of an MPP in the presence of grazing flow. This model was subsequently verified through numerical simulations and experiments.[25, 26]. Wu et al. [27] conducted an experimental investigation into the aeroacoustic properties of single-layer perforated liners under the presence of both bias and grazing flow at low Mach numbers.

The stringent standards associated with modern aviation noise emissions contribute to the growing demands placed on the acoustic performance of aircraft engine liners [29–32]. Traditional perforated plate over honeycomb (POHC) liners have been broadly utilized for the attenuation of noise generated by turbofan engines. The most

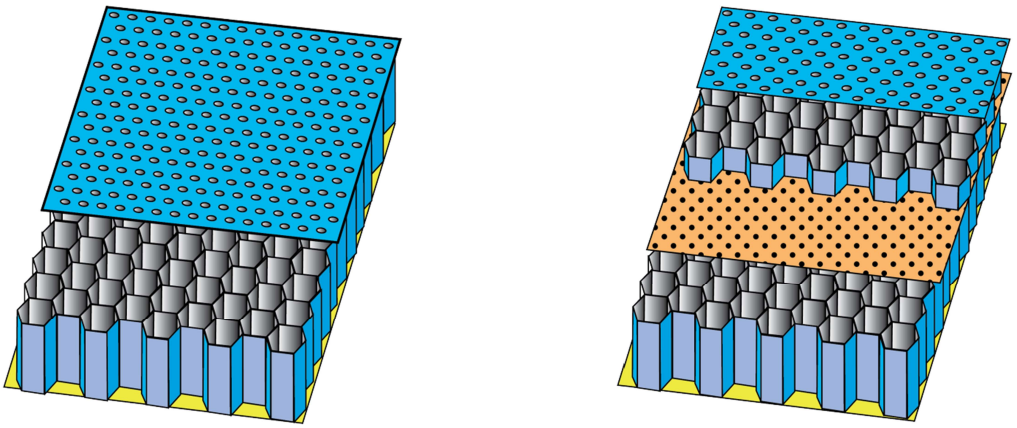

(a) SDOF (b) DDOF

Fig. 1 SDOF liner and DDOF liner [28].

prevalent POHC acoustic liners are available in two configurations: the Single-Degree-of-Freedom (SDOF) liner and the Double-Degree-of-Freedom (DDOF) liner (see Fig. 1). The SDOF liner typically comprises a honeycomb-like cavity structure, a solid back plate, and a perforated facesheet. However, this liner design yields a relatively narrow sound absorption spectrum. The DDOF liner, on the other hand, is essentially an SDOF arrangement with an embedded porous septum or perforated plate. While the DDOF liner does expand the sound absorption bandwidth, its structure becomes more complex and its weight increases. Additionally, the DDOF liner generally necessitates more space compared to the SDOF liner.

In this paper an advancement over POHC liners and the state-of-the-art in MPPA research are presented. The investigated MC-MPPA technology is simple, lightweight and robust in structure and has excellent sound absorption performance [16]. The shape is rectangular in shape allowing it to be easily tessellated. The breakthrough is in employing a graph-theory-based, two-point impedance method (TpIM) [16, 17, 33, 34] to model the system allowing the MC-MPPA to be optimized to have maximum sound absorption in a chosen frequency range. The graph theory approach is a breakthrough as an equivalent circuit model [15] approach could not be used with such complex models, refer to the discussion in [17].

The primary objectives of the present investigation include the following components: (1) To advance the previously proposed MC-MPPA with micro-perforated adjoining panels and constant sub-chamber depth (denoted as MC-MPPA-I) [16], the present study develops a rectangular MC-MPPA incorporating non-perforated adjoining panels and variable sub-chamber depth (denoted as MC-MPPA-II). (2) To devise optimized configurations for MC-MPPA-I and MC-MPPA-II utilizing the two-point impedance method, demonstrating remarkable broadband low-frequency normal sound incidence absorption capabilities. (3) To validate the proposed MC-MPPA-I and MC-MPPA-II designs through impedance tube experiments and numerical analysis. (4) To obtain the exact Cremer impedance in rectangular lined ducts based on the classical boundary condition. (5) To optimize the proposed MC-MPPA-I and MC-MPPA-II models under grazing flow conditions, utilizing the two-point impedance method and exact Cremer impedance for broadband and high amplitude sound transmission loss. (6) To numerically validate the acoustic performance of the proposed MC-MPPA-I and MC-MPPA-II under grazing acoustic incidence conditions.

III. MC-MPPA Design

In the present study, we examine two variations of MC-MPPAs: MC-MPPA-I and MC-MPPA-II. Both MC-MPPA-I and MC-MPPA-II designs under examination comprises a complex acoustic system composed of multiple micro-perforated panels (MPPs) and air cavities (ACs).

- MC-MPPA-I: is a rectangular multi-chamber micro-perforated panel absorber (MC-MPPA) with micro-perforated adjoining panels and constant sub-chamber/core depth. As the sub/chambers in the core are interconnected through micro-perforations, this is a non-locally reacting liner. Previous research [16] has demonstrated that the MC-MPPA-I is a highly promising deep subwavelength absorber, displaying high amplitude broadband sound

absorption of planar acoustic waves in impedance tube evaluations. As normal incidence conditions have been already examined for this design, in this paper, the sound absorption capabilities of the MC-MPPA-I under grazing acoustic incidence conditions are explored in order to further understand its capabilities.

- MC-MPPA-II: is a rectangular multi-chamber micro-perforated panel absorber (MC-MPPA) with non-perforated adjoining panels but with variable sub-chamber depth. This MPPA is considered to be a multi-chamber (MC) variation on an MPPA, or a SDOF POHC liner, for example, as each sub-chamber can have a unique depth. Similarly, the characteristics of the perforations in the face-plate (hole count, diameter, porosity) can vary from one sub-chamber to another. This variation is examined as it may be easier to manufacture than the design which requires internal perforations. As this is an original design, both the normal and grazing acoustic incidence conditions are examined here.

A. MC-MPPA-I

The MC-MPPA-I is shown in Fig. 2 (a) and (b). It is sub-divided into 3×3 chambers, wherein each sub-chamber has an identical depth, D, and adjacent sub-chambers are separated by micro-perforated panels.

The overall configuration of this MC-MPPA-I is rectangular, facilitating its tessellation for practical industrial applications. The length of the investigated MC-MPPA-I is designated as L, and the width is designated as W. The thickness of the top and interior MPPs are designated as τ_t and τ_i, respectively. In the present study, the thickness of all the top MPPs are equal to one another, as are the thicknesses of all the internal MPPs. However, both τ_t and τ_i can be different to one another. The overall height of MC-MPPA-I is obtained by summing the thickness of the top MPP, τ_t, with the depth of the air cavity, D.

In this paper, the top MPPs of MC-MPPA-I are denoted as $\text{MPP}_{t1(1)}$, $\text{MPP}_{t1(2)}$, $\cdots$, $\text{MPP}_{t1(9)}$, respectively.The internal MPPs are denoted as $\text{MPP}_{i(1)}$, $\text{MPP}_{i(2)}$, $\cdots$, $\text{MPP}_{i(12)}$, respectively using a serpentine naming method [16].

B. MC-MPPA-II

MC-MPPA-II is shown in Fig. 2 (c) and (d). The MC-MPPA-II structure under investigation is divided into a 3×3 chambers, each with distinct depths and separated by non-perforated partitions. The MC-MPPA-II under examination possesses equivalent dimensions for both length and width in comparison to MC-MPPA-I, which are also designated as L and W respectively. The thickness of the top MPPs of the MC-MPPA-II is equal to that of MC-MPPA-I and is also symbolized as τ_t. The thickness of the non-perforated adjacent panels of the MC-MPPA-II is equivalent to that of the interior MPPs of the MC-MPPA-I and is denoted as τ_i. The overall height of the MC-MPPA-II is attained through the addition of the thickness of the top MPP, τ_t, and the depth of the deepest sub-chamber.

In this paper, the top MPPs of MC-MPPA-II are denoted as $\text{MPP}_{t2(1)}$, $\text{MPP}_{t2(2)}$, $\cdots$, $\text{MPP}_{t2(9)}$, respectively. The depths of the air cavities within the structure are designated as $D_{(1)}$, $D_{(2)}$, $\cdots$, $D_{(9)}$, respectively, where the maximum depth is defined as $D_{\max}$. In the subsequent discussion of MC-MPPA-II's sub-chamber depth within this paper, the reference pertains to the depth of its deepest sub-chamber $D_{\max}$.

The constitutive parameters of both MC-MPPA-I (see Table 1) and MC-MPPA-II (see Table 2) under investigation, with four controlling parameters for micro-perforated panels defined as follows:

- panel thickness τ;
- perforation diameter d;
- perforation porosity φ (ratio of micro-perforated area to total area);
- perforation number n.

IV. Analytical Models

In this paper, we use the following three analysis methods: Two-point impedance method (TpIM), Cremer impedance and MPP impedance under grazing flow conditions.

- **Two-point impedance method:** The two-point impedance method [16–18, 33, 34] is a viable approach to determine the impedance between any two nodes in a complex impedance network, regardless of the circuit's planarity. Although traditional equivalent circuit models can be applied to simple circuits, they are inadequate for more complex non-planar circuits required by higher order MC-MPPAs. Therefore, the use of the two-point impedance method is recommended for such circuits.
- **Cremer Impedance:** The method of Exact Cremer Impedance is named after its creator, L. Cremer [35], and is highly effective in providing a reasonable estimate of the optimal impedance for a particular set of duct parameters.

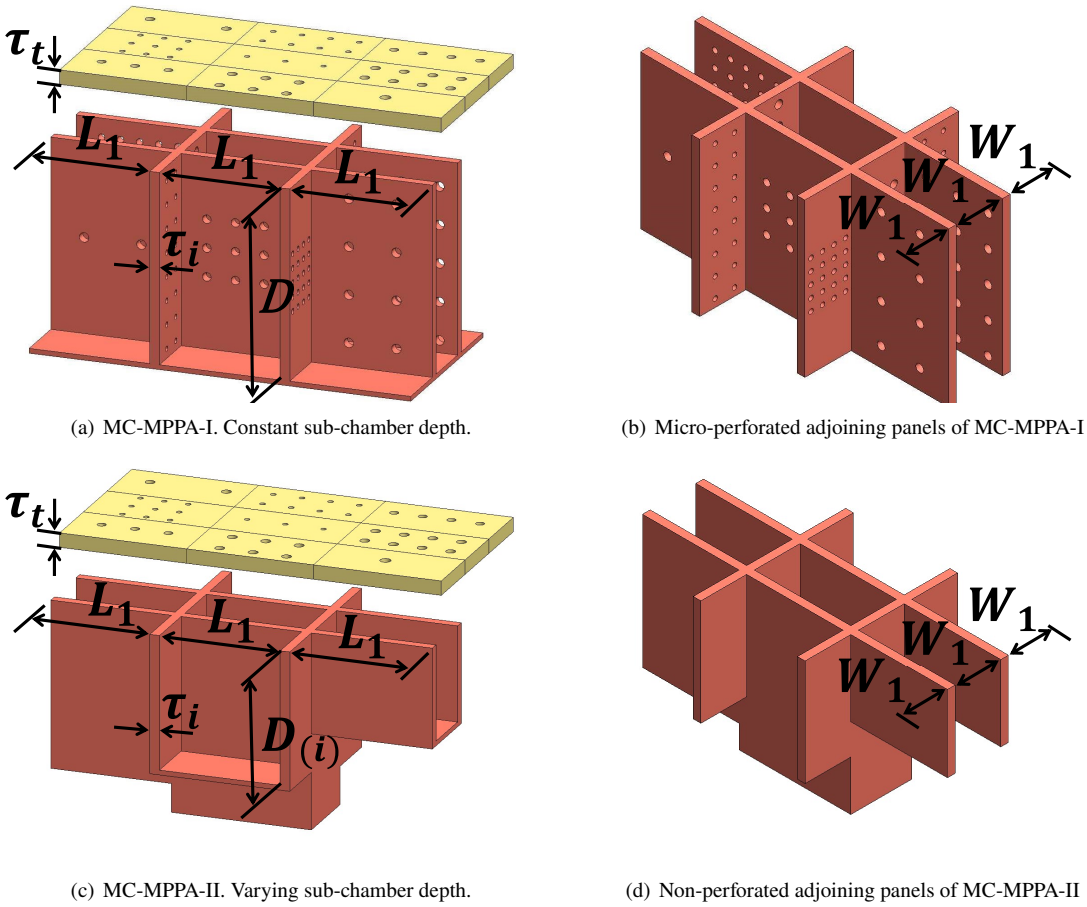

(a) MC-MPPA-I. Constant sub-chamber depth.

(b) Micro-perforated adjoining panels of MC-MPPA-I

(c) MC-MPPA-II. Varying sub-chamber depth.

(d) Non-perforated adjoining panels of MC-MPPA-II

Fig. 2 Geometric layout of the MC-MPPA-I and MC-MPPA-II structures that are the focus of the current study, where L_1 represents $\frac{L-2\tau_i}{3}$ and W_1 represents $\frac{W-2\tau_i}{3}$.

Location of MPPs	Symbol of MPPs	Panel thickness	Perforation diameter	Perforation porosity	Perforation number	Sub-chamber depth
Top surface of MC-MPPA-I	$\mathrm{MPP}_{t1(1)}$	τ_t	$d_{t1(1)}$	$\varphi_{t1(1)}$	$n_{t1(1)}$	D
	$\mathrm{MPP}_{t1(2)}$		$d_{t1(2)}$	$\varphi_{t1(2)}$	$n_{t1(2)}$	
	$\mathrm{MPP}_{t1(3)}$		$d_{t1(3)}$	$\varphi_{t1(3)}$	$n_{t1(3)}$	
	$\vdots$		$\vdots$	$\vdots$	$\vdots$	
	$\mathrm{MPP}_{t1(9)}$		$d_{t1(9)}$	$\varphi_{t1(9)}$	$n_{t1(9)}$	
Internal walls of MC-MPPA-II	$\mathrm{MPP}_{i(1)}$	τ_i	$d_{i(1)}$	$\varphi_{i(1)}$	$n_{i(1)}$	
	$\mathrm{MPP}_{i(2)}$		$d_{i(2)}$	$\varphi_{i(2)}$	$n_{i(2)}$	
	$\mathrm{MPP}_{i(3)}$		$d_{i(3)}$	$\varphi_{i(3)}$	$n_{i(3)}$	
	$\vdots$		$\vdots$	$\vdots$	$\vdots$	
	$\mathrm{MPP}_{i(12)}$		$d_{i(12)}$	$\varphi_{i((12)}$	$n_{i(12)}$	

Table 1 The parameters that define the acoustic behavior of the MC-MPPA-I under examination.

The Cremer Impedance is commonly used in duct acoustic applications, such as the design of mufflers for internal

Location of MPPs	Symbol of MPPs	Panel thickness	Perforation diameter	Perforation porosity	Perforation number	Sub-chamber depth
Top surface of MC-MPPA-II	$\mathrm{MPP}_{t2(1)}$	τ_t	$d_{t2(1)}$	$\varphi_{t2(1)}$	$n_{t2(1)}$	$D_{(1)}$
	$\mathrm{MPP}_{t2(2)}$		$d_{t2(2)}$	$\varphi_{t2(2)}$	$n_{t2(2)}$	$D_{(2)}$
	$\mathrm{MPP}_{t2(3)}$		$d_{t2(3)}$	$\varphi_{t2(3)}$	$n_{t2(3)}$	$D_{(3)}$
	$\vdots$		$\vdots$	$\vdots$	$\vdots$	$\vdots$
	$\mathrm{MPP}_{t2(9)}$		$d_{t2(9)}$	$\varphi_{t2(9)}$	$n_{t2(9)}$	$D_{(9)}$

Table 2 The parameters that define the acoustic behavior of the MC-MPPA-II under examination.

combustion engines [36–39]. Although it was originally developed for scenarios without flow, it has been further refined and successfully applied in situations with flow [40].

- **MPP impedance under grazing flow conditions:** Grazing flows can significantly complicate the prediction of acoustic behaviors of MPPs due to the complex interplay between the acoustic waves and the flow field inside and in close proximity to the perforation holes. Åbom et al. [22–24] investigated the effects of grazing flow on the impedance of MPPs. They also created analytical models for MPPs with circular and slit-shaped perforation holes under grazing flow conditions and successfully verified their accuracy through experimental validation.

This paper utilizes the TpIM method to calculate the acoustic impedance of the designed MC-MPPA under normal acoustic incidence. The situation becomes slightly more complicated under grazing acoustic incidence. Nevertheless, we still apply the TpIM method to obtain the acoustic impedance of the MC-MPPA and match it with the optimal acoustic impedance of the target duct obtained via the Cremer impedance method. In calculating the acoustic impedance of the MC-MPPA, we consider the impact of flow on the MPP impedance by utilizing the MPP under grazing flow conditions. Currently, we are solely considering grazing acoustic incidence without any flow, and thus, we assign the Mach number $M = 0$ in the methods of Cremer impedance and MPP impedance under grazing flow conditions. When the flow is introduced, we simply need to incorporate the specific Mach number in the aforementioned methods.

A. Analytical modeling of a MC-MPPA using a two-point impedance method (TpIM)

In the case of normal incidence, we chose the boundary condition of the interior perforated thin panel provided by COMSOL (in which the losses caused by heat conduction are negligible) to calculate the impedance of the MPP [15–18]. COMSOL'S acoustic impedance, Z_{mpp}, of each MPP when exposed to sound under normal incidence can be determined using Eq. (1). As previously demonstrated in a numerical study, this approach has been found to be in close agreement with a fully resolved representation of perforated holes in a COMSOL model [15].

$$\frac{Z_{\mathrm{mpp,Comsol}}}{\rho_0 c_0} = -\left(\frac{\mathrm{i}\omega}{c_0\varphi}\frac{\tau + 8d\Lambda(\varphi)/3\pi}{Y_v}\right) \tag{1}$$

where i is the imaginary unit, ρ_0 represents the density of air and c_0 symbolizes the speed of sound in air. The angular frequency is expressed as $\omega = 2\pi f$ where f is the frequency in Hertz. The term Y_v is given by

$$Y_v = \frac{J_2\left(k_v d/2\right)}{J_0\left(k_v d/2\right)}, \quad k_v = \sqrt{-\frac{\mathrm{i}\omega\rho_0}{\mu}} \tag{2}$$

where J_n is the nth order Bessel function and μ is the dynamic viscosity of air.

The hole-to-hole interaction, if any, is determined by the Fok function, $\Lambda(\varphi)$, which is expressed by

$$\Lambda(\varphi) = \sum_{n=0}^{8} a_n(\sqrt{\varphi})^n \tag{3}$$

where the following first eight coefficients [15] are used in this study: $a_0 = 1$, $a_1 = -1.4092$, $a_2 = 0$, $a_3 = 0.33818$, $a_4 = 0$, $a_5 = 0.06793$, $a_6 = -0.02287$, $a_7 = 0.063015$ and $a_8 = -0.01614$.

Regarding the air cavities within the investigated MC-MPPA-I and MC-MPPA-II, the acoustic impedance, Z_{ac}, of each AC can be calculated by Eq. (4).

$$Z_{\mathrm{ac}} = -\mathrm{i}\rho_0 c_0 \cot\left(\frac{\omega D}{c}\right) \tag{4}$$

In this study, the two-impedance method (TpIM) is employed to calculate the impedance of both MC-MPPA-I and MC-MPPA-II. Fig. 3 shows the investigated MC-MPPA-I and MC-MPPA-II designs from Fig. 2 represented schematically as bipyramid molecular structures where the yellow branches represent the acoustic impedances of the top MPPs, the red branches represent the acoustic impedances of internal MPPs and the green branches represent the acoustic impedances of the air cavities themselves. It has been shown in previous studies that, unlike the equivalent circuit method approach, the TpIM can be used to determine the impedance between any two nodes in a complex impedance network whether the circuit is planar or not [16–18, 33, 34].

Based on this molecular structure, the following Laplace matrix $\mathbf{L}$ can be constructed:

$$\mathbf{L} = \begin{pmatrix} y_{11} & -y_{12} & \dots & -y_{1\mathcal{N}} \\ -y_{21} & y_{22} & \dots & -y_{2\mathcal{N}} \\ \vdots & \vdots & \ddots & \vdots \\ -y_{\mathcal{N}1} & -y_{\mathcal{N}2} & \dots & y_{\mathcal{N}\mathcal{N}} \end{pmatrix} \tag{5}$$

where $\mathcal{N} = (3\times3)+2$ is the number of nodes, y_{ij} is the admittance between nodes i and j, and $y_{ij} = y_{ji} = 1/Z_{ij}$ $(i \neq j)$, with Z_{ij} being the acoustic impedance between nodes i and j.

The diagonal elements of the Laplace matrix $\mathbf{L}$ can be given by

$$y_{ii} \equiv \sum_{j=1}^{\mathcal{N}} y_{ij} \quad i \neq j \tag{6}$$

Use of the Laplace matrix, $\mathbf{L}$, allows us to form the Hermitian matrix $\mathbf{L}^\dagger\mathbf{L}$, which can be diagnolised and where $\dagger$ denotes the hermitian conjugation. In order to calculate the impedance of the network represented by the Laplace matrix, the following eigenvalue equation must solved:

$$\mathbf{L}^\dagger\mathbf{L}\psi_\beta = \eta_\beta\psi_\beta, \quad \eta_\beta \geqslant 0, \quad \beta = 1, 2, \dots, \mathcal{N} \tag{7}$$

where η_β and ψ_β are the eigenvalues and eigenvectors of $\mathbf{L}^\dagger\mathbf{L}$ respectively. There then exist eigenvalues of $\mathbf{L}$, which can be given by

$$\lambda_\beta = \psi_\beta^\dagger \mathbf{L}\psi_\beta \tag{8}$$

Finally, the acoustic impedance between any two nodes i and j in the network is given by

$$Z_{ij} = \sum_{\beta=2}^{\mathcal{N}} \frac{1}{\lambda_\beta}\left(\psi_\beta(i) - \psi_\beta(j)\right)^2 \tag{9}$$

Given this value, the specific impedance z_{ij} can be calculated from Eq. (10)

$$z_{ij} = Z_{ij}S \tag{10}$$

where S is the area of normal incidence of the sound wave.

The reflection coefficient R, which is a function of the impedance, is given by the expression

$$R = \frac{z_{ij} - \rho_0 c_0}{z_{ij} + \rho_0 c_0} \tag{11}$$

and from this the normal incidence sound absorption coefficient α can be calculated according to

$$\alpha = 1 - |R|^2 \tag{12}$$

Further detail and illustrations of how the TpIM can be used to simplify complex acoustic circuits can be found in Davis et al. [17] and Wang and Bennett [16].

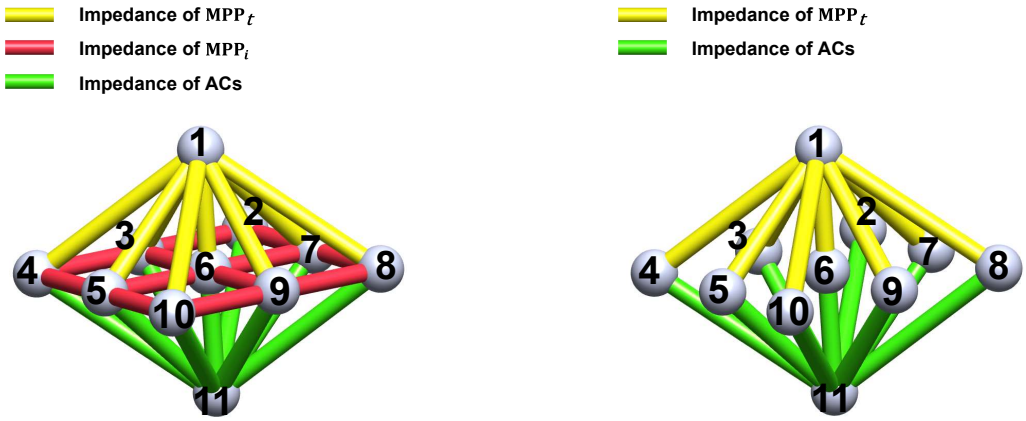

(a) MC-MPPA-I (b) MC-MPPA-II

Fig. 3 Molecular structure of the investigated MC-MPPA-I and MC-MPPA-II in this paper.

B. Exact Cremer impedance in rectangular lined ducts based on the classical boundary condition.

Figure 4 illustrates the placement of an acoustic liner with an impedance Z on a single side of a 2-D rectangular duct, where a rigid wall is situated on the opposing side of the duct. The grazing flow within the duct remains at a constant Mach number, M. The Cremer impedance wasinitially proposed by Cremer [35] for no-flow conditions and for rectangular ducts. Tester [40] extended the theory for flow and for circular ducts with a focus on high frequencies and well-cut on modes. The Cremer impedance can offer a reasonable estimate of the optimal impedance for a particular set of duct parameters (M, k_x, k_y and H) [36–39]. By confining the analysis solely to 1-D symmetric modes, the acoustic field can be expressed as [38]:

$$p(x, y) = A\Psi\left(k_y y\right) \exp\left(-ik_x x\right) \tag{13}$$

Here, A and Ψ correspond to the mode amplitude and shape, respectively. The variables k_x and k_y represent the x-axis and y-axis components of the wavenumber k, respectively. Their relationship can be expressed as:

$$k_x/k = -\frac{M}{1-M^2} \pm \frac{\sqrt{1-\left(k_y/k\right)^2\left(1-M^2\right)}}{1-M^2} \tag{14}$$

where $k = 2\pi f/c$ is the wavenumber. It is necessary to select branch ($\pm$) of the root to ensure that the modes are damped in the positive x direction.

In previous related studies [39, 41–44], the Ingard-Myer boundary condition (IM B.C.) [45, 46], which postulates the continuity of normal acoustic displacement across a boundary layer of infinitesimal thickness, has been widely used. However, this results in a negative real part of the impedance at low frequencies, rendering the solution in the upstream direction invalid. Åbom and Jacob [38, 47] noted that replacing the IM B.C. with the classical boundary condition (Classical B.C.), i.e., continuity of pressure and normal velocity can eliminate the aforementioned issue. Thus the Classical B.C. is adopted as the boundary layer condition in this current study. The dispersion equation for the modes in a rectangular duct can be derived as follows, by employing Eq. (13) and the linearized equation of motion [39]:

$$\left(1 - M\frac{k_x H}{kH}\right)^{-1} \cdot k_y H \cdot \tan\left(k_y H\right) = ikH\frac{\rho_0 c}{Z} \tag{15}$$

When considering a specific liner impedance Z, Helmholtz number ($He = kH$), and Mach number, the transverse wave number $k_y H$ can be obtained by solving Eq. (15). According to Cremer [35] and Tester [40], to obtain an exceptional point where mode merging occurs, the first derivative of the dispersion equation must be zero at the root.

$$\frac{\partial}{\partial\left(k_y H\right)}\left[\left(1 - M\frac{k_x H}{kH}\right)^{-1} \cdot k_y H \cdot \tan\left(k_y H\right)\right] = 0 \tag{16}$$

The "exact" solution to the complete branch point equation is derived with the introduction of a mean flow related term.

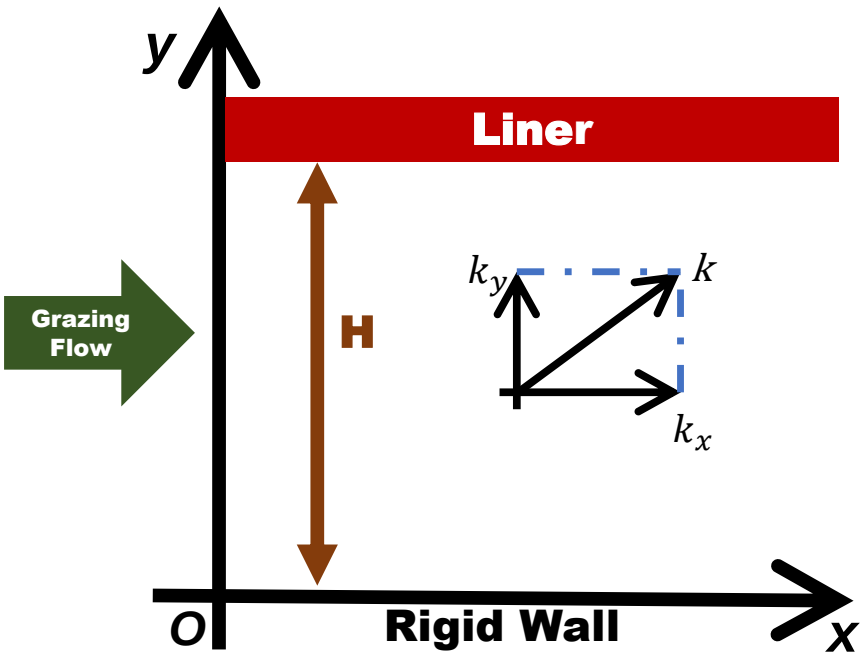

Fig. 4 A schematic representation of a liner in a rectangular duct with a grazing flow. The height of the duct is H. The components of the wavenumber k on the x and y axes are k_x and k_y respectively.

$$Z_{\mathrm{cr}}\,|_M = \frac{\mathrm{i}\pi\,(1 - M_x k_x/k)}{(k_y)\tan(k_y H)} \cdot \frac{kH}{\pi} \tag{17}$$

where the normalized Cremer impedance, symbolized by $Z_{\mathrm{cr}}\,|_M$, delineates the theoretical apex of acoustic damping of a rectangular duct (see Fig. 4) in the presence of a uniform, grazing flow at a certain Mach number. Fig. 5 illustrates the theoretically predicted normalized exact Cremer impedance, where the real component is denoted by "Re" and the imaginary component by "Im", based on the classical boundary condition. It should be indicated that, under conventional boundary conditions, the real component of the Cremer impedance remains positive even at low frequencies. These results are in agreement with the findings previously reported in Åbom and Jacob [38, 47].

The transmission loss (TL) per duct height can be calculated with

$$\mathrm{TL} = 20\log_{10}\left|\exp\left(-\mathrm{Im}\left((k_x H)_{\mathrm{opt}}\right)\right)\right| \tag{18}$$

C. Impedance Model of an MPP under grazing flow conditions

According to Maa's theory [12–14], the acoustic impedance of an MPP, $Z_{\mathrm{mpp,Maa}}$ can be expressed as:

$$Z_{\mathrm{mpp,Maa}} = R + \mathrm{i}\chi \tag{19}$$

where the acoustic resistance of MPP is denoted by R, while the acoustic reactance is represented by χ. However, there is currently no universally recognized formula for calculating the reactance and resistance of an MPP when the effects of grazing flow are taken into consideration. Åbom et al. [22–24] have proposed a formula for the reactance and resistance of an MPP in grazing flow. In their studies, R can be calculated by Eq. (20) and χ can be calculated by Eq. (21), respectively.

$$R = \mathrm{Re}\left[\frac{\mathrm{i}\omega t}{\sigma c}\left[1 - \frac{2}{k\sqrt{-\mathrm{i}}}\frac{J_1\left(k\sqrt{-\mathrm{i}}\right)}{J_0\left(k\sqrt{-\mathrm{i}}\right)}\right]^{-1}\right] + \frac{2\alpha' R_s}{\sigma c} + \frac{|u_h|}{\sigma c} + \beta\frac{|M|}{\sigma} \tag{20}$$

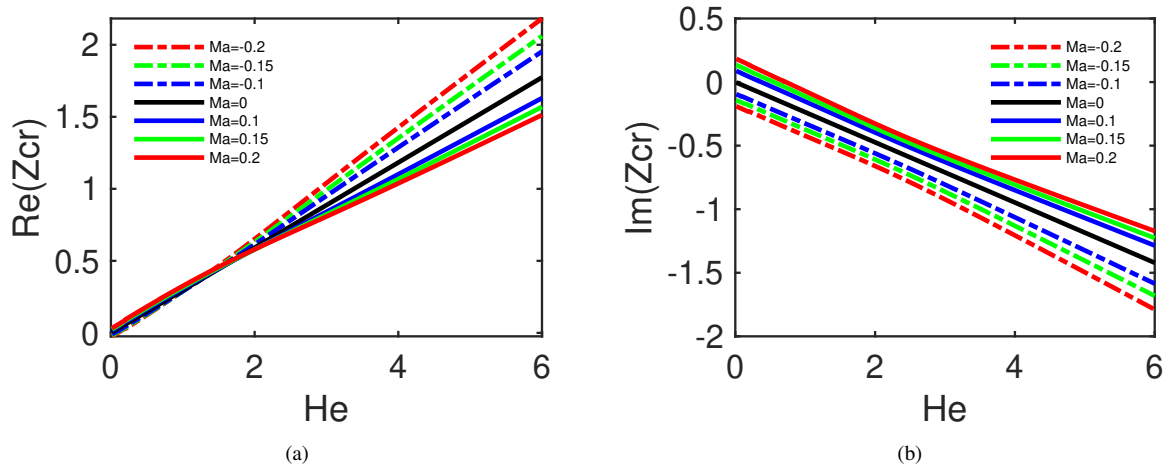

(a) (b)

Fig. 5 Theoretically predicted normalized exact Cremer impedance in a rectangular ducts, (a) resistance of Z_{cr} at different Mach numbers, (b) reactance of Z_{cr} at different Mach numbers.

and

$$\chi = \mathrm{Im}\left[\frac{\mathrm{i}\omega t}{\sigma c}\left[1 - \frac{2}{K\sqrt{-\mathrm{i}}}\frac{J_1\left(k\sqrt{-\mathrm{i}}\right)}{J_0\left(k\sqrt{-\mathrm{i}}\right)}\right]^{-1}\right] + \frac{\delta\omega F_\delta\left(1 + \frac{|u_h|}{\sigma c}\right)^{-1}}{\sigma c} \tag{21}$$

where

$$F_\delta = \frac{1}{1 + 2000|M|^3} \tag{22}$$

and

$$\beta = 0.15 \pm 0.0125(\mathrm{std}) \tag{23}$$

F_δ and β represent the effect of this flow on reactance and resistance respectively. The shear wavenumber, K is defined as

$$K = d\sqrt{\frac{\omega}{4\mu}} \tag{24}$$

The surface resistance, R_s is defined as

$$R_s = d\sqrt{\frac{\omega\mu}{2}} \tag{25}$$

The edge-related coefficient, α' and the mass end correction coefficient, δ are defined as Eq. (26) and Eq. (27), respectively.

$$\alpha' = 5.08K^{-1.45} + 1.7 \tag{26}$$

$$\delta = \frac{d}{2}\left[0.97\exp\left(-0.2K\right) + 1.54\right] \tag{27}$$

V. Optimization Strategy

A. Under normal acoustic incidence conditions

The absorption coefficients of standard MPPAs can be high for relatively arbitrarily chosen parameters but the frequency responses tend to be quite narrow, and typically become more so with decreasing frequency range. One of the main objectives of applying the TpIM to the MC-MPPA technology is to provide an analytical model, and with that model, optimize the absorbers so that they are as efficient as possible for a fixed set of parameters.

Considering a target sound spectrum described by an auto-spectral density function $G_{xx}(\omega)$, the sound power reduction that a sound absorber with an absorption spectrum $\alpha(\omega)$ would achieve in Decibels can be written as:

$$C_\alpha = 10\log_{10}(1 - c_\alpha) \tag{28}$$

where c_α is the overall absorption coefficient weighted by the sound spectrum of the targeted noise source:

$$c_\alpha = \frac{\left(\sum_{\omega_1}^{\omega_2} \alpha(\omega) G_{xx}(\omega)\right)}{\left(\sum_{\omega_1}^{\omega_2} G_{xx}(\omega)\right)} \tag{29}$$

where $\omega_1 = 2\pi f_1$ and $\omega_2 = 2\pi f_2$, with f_1 and f_2 being the lower and upper limits of the frequency range of interest. The absorption coefficient, $\alpha(\omega)$, is calculated from Eq. (12) using the TpIM for both MC-MPPA-I and MC-MPPA-II in Fig. 2 for normal acoustic incidence.

The target sound spectrum is the noise that is required to be attenuated and to which the optimization algorithm attempts to match. This spectrum can be arbitrary and the method has been shown to work well with both tonal and white noise [15, 17, 18]. In the current study, the target sound source is white noise, $G_{xx}(\omega) \equiv 1$.

The sound power reduction factor, C_α, provides a suitable cost function that can be minimized in an optimization routine in order to generate the parameter set for an optimal MC-MPPA. C_α can be expressed as a function of the geometric parameter set chosen for the optimization algorithm.

An optimisation method based on Sequential Quadratic Programming (SQP) was used to minimise the cost function. SQP is a classical iterative method for constrained nonlinear optimization which applies to optimization issues where the objective function and the constraints are twice continuously divisible.

Further detail and illustrations of this optimisation can be found in Wang and Bennett [16].

Both MC-MPPA-I and MC-MPPA-II are optimized under normal acoustic conditions. The optimized designs are called MC-MPPA-I-N and MC-MPPA-II-N respectively, where N stands for normal. Numerical and experimental analysis will be performed on these specific geometries.

B. Under grazing acoustic incidence conditions

In grazing acoustic incidence, the acoustic impedance $Z_{\mathrm{MC-MPPA}}$ of both MC-MPPA-I and MC-MPPA-II can once again be calculated using Eq. (9) using TpIM. However, in grazing conditions, the impedance is different to that in normal incidence and also varies with the flow Mach number when a flow is present. The main difference in the approach to the normal incidence model is that Eqs. (19)-(21) are used to calculate the surface impedance of the top MPP. For MC-MPPA-I, the impedance of the internal MPPs are still calculated with COMSOL's interior perforated thin panel boundary condition, i.e., Eq. (1).

Regarding the optimization, the strategy is to optimize the MC-MPPA such that its acoustic impedance matches the Cremer impedance, as defined by Eq. (17), i.e.,

$$Z_{\mathrm{Cr}} = Z_{\mathrm{MC-MPPA}} \tag{30}$$

While Eq. (30) is useful for determining the optimal design of the MC-MPPA for a specific target frequency, it may not be adequate to obtain a globally optimal solution across the entire range of target frequencies. To overcome this limitation, we propose a modification of Eq. (30) in the form of Eq. (31), which serves as a cost function for optimization, allowing for the identification of the optimal design of the MC-MPPA across the frequency range.

$$J = \frac{1}{\omega_2 - \omega_1} \int_{\omega_1}^{\omega_2} \sqrt{[\mathrm{Re}(Z_{\mathrm{Cr}}) - \mathrm{Re}(Z_{\mathrm{MC-MPPA}})]^2 + [\mathrm{Im}(Z_{\mathrm{Cr}}) - \mathrm{Im}(Z_{\mathrm{MC-MPPA}})]^2}\, \mathrm{d}\omega \tag{31}$$

where $\omega_1 = 2\pi f_1$, $\omega_2 = 2\pi f_2$, f_1 and f_2 are the lower and upper limits of the target frequency range respectively. Eq. (31) can be employed to ensure that the acoustic impedance of the MC-MPPA matches the Cremer impedance to the greatest extent possible across the frequency range $[f_1\ f_2]$. Subsequently, the built-in *fmincon* SQP algorithm in Matlab is utilized to minimize this cost function and obtain the optimized parameters of the MC-MPPA.

Both MC-MPPA-I and MC-MPPA-II are optimized under grazing acoustic conditions. The optimized designs are called MC-MPPA-I-G and MC-MPPA-II-G respectively, where G stands for grazing. Numerical analysis will be performed on these specific geometries.

VI. Experimental Setup

In this paper, experiments are performed on both the MP-MPPA-I and MP-MPPA-II designs of Fig. 2 but only for normal acoustic impedance.

A. Rectangular impedance tube

The normal incidence sound absorption coefficients of MC-MPPA-I and MC-MPPA-II were measured experimentally using a rectangular normal impedance tube with an internal cross-section of 80 mm × 50 mm, as depicted in Fig. 6. The experimental configuration adhered to the guidelines stipulated in the ISO 10534-2:1998 Standard [48]. The plane wave cut-off frequency of the duct is approximately 2100 Hz. In order to generate planar sound waves, two 150 W BMS 4591 2" compression drivers were positioned at one end of the tube, while the test samples were mounted at the opposite end. As the low-frequency response of the compression drivers utilized in this experiment is limited, the lower frequency limit for sound absorption measurements using this apparatus is set at 200 Hz. Therefore, the experimental results presented in this study will be restricted to frequencies above this lower limit. The measurements were conducted utilizing G.R.A.S 40PH microphones, which possess a flat frequency response of 20 Hz to 20 kHz, thereby surpassing the frequency range of the acoustic drivers and the analysis conducted in this experiment.

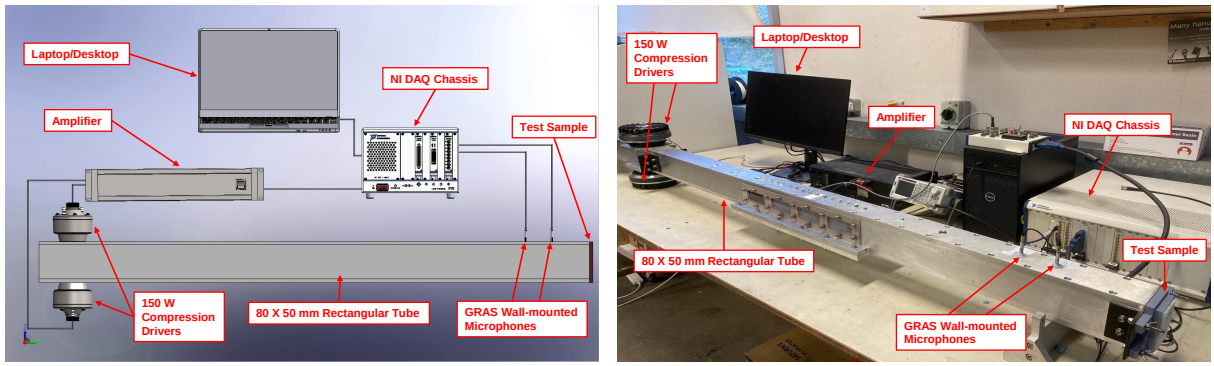

(a) Illustration of the rectangular impedance tube used to measure MC-MPPA's sound absorption coefficients

(b) Photo of this rectangular impedance tube

Fig. 6 Experimental rig test set up [16].

B. MC-MPPA-I test sample

A test sample of the MC-MPPA-I-N design is shown in Fig. 7. This test-piece was optimized for normal acoustic incidence and fabricated using a Masked Stereolithography (MSLA) 3D printing technique and a standard photopolymer resin (color: grey) with a wavelength of 405 nm. The target spectrum for the optimization was white noise, with a perforation diameter range of 0.5-1.0 mm, a perforation porosity range of 0-5%, a working frequency range of 200-2000 Hz, and a sub-chamber depth of 20 mm. The optimized geometric parameters as obtained from the optimization procedure of test sample MC-MPPA-I-N are presented in Table 3 in Appendix IX.A.

-

C. MC-MPPA-II test sample

Similarly, a test-piece of MC-MPPA-II-N optimized for normal acoustic incidence is shown in Fig. 8. The uppermost MPP, which serves as the faceplate, (see Fig. 8(a)) was constructed using the Masked Stereolithography (MSLA) 3D printing technique and a Standard Photopolymer Resin (color: grey) activated by a 405 nm wavelength light source. The sub-chambers, or core, (see Fig. 8(b)) in MC-MPPA-II-N, which range in depth, were produced using the Fused Deposition Modelling (FDM) 3D printing technique and Polylactic Acid (PLA) filament. The optimized geometric parameters, as obtained from the optimization procedure outlined in Section V of the test sample MC-MPPA-II-N within the framework of the rectangular impedance tube experiments, are presented in Table 4 in Appendix IX.A.

Additionally, for both MC-MPPA-I-N and MC-MPPA-II-N test samples, in order to conform to the dimensions of the impedance tube (80 × 50 mm), two identical test samples (with dimensions of L = 50 mm and W = 40 mm) were

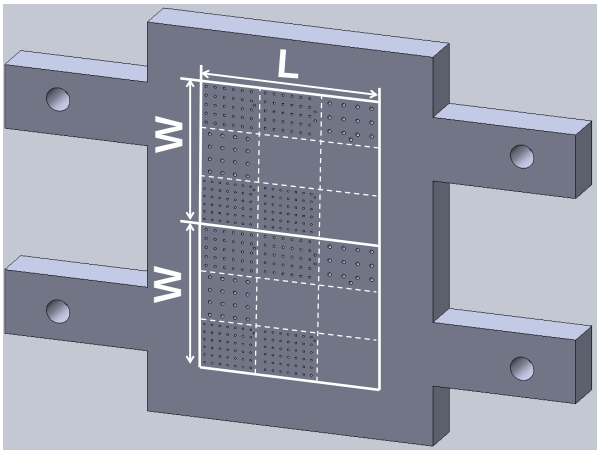

(a) An isometric view of MC-MPPA-I-N showing the perforations in the MPPt (integrated face plate) on the side exposed to the acoustic plane waves in the impedance tube

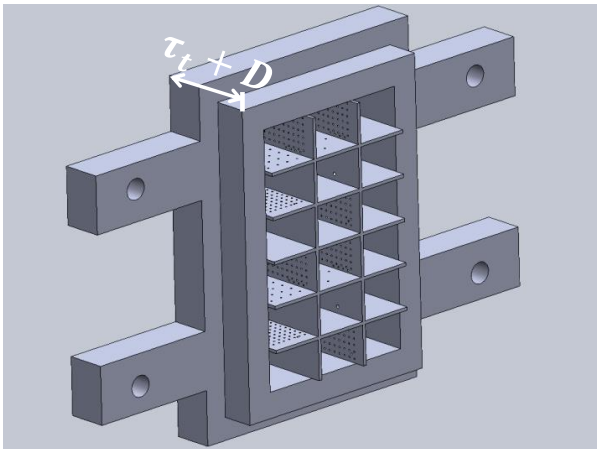

(b) A perspective of the internal perforated panels, wherein the number and porosity of holes may vary from panel to panel. A solid aluminum backplate is attached to this side.

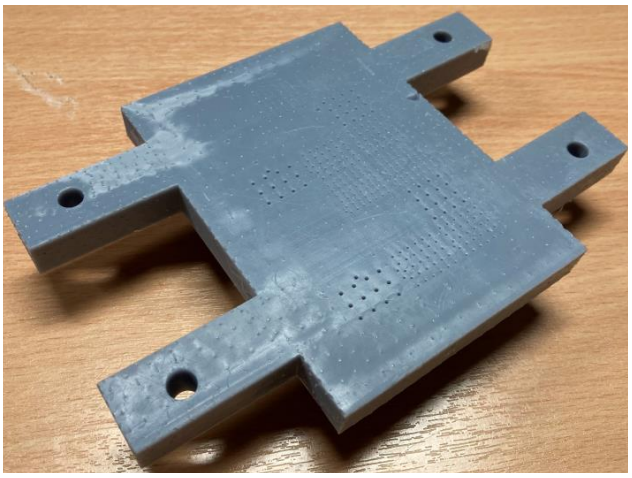

(c) Photograph of MC-MPPA-I-N with rig attachment flanges.

Fig. 7 CAD and photo images of the MC-MPPA-I-N test-piece. D=20 mm [16].

printed side-by-side (see Figs. 7 and 8). This arrangement has the benefit of reducing manufacturing errors during the 3D-printing process, as the parallel arrangement of two identical MC-MPPAs for sound absorption measurements is equivalent to fabricating the same MC-MPPA design twice and measuring sound absorption twice.

The printing accuracy of the 3D-printed apertures in both the MC-MPPA-I-N and MC-MPPA-II-N samples was assessed using the Dino-Lite Premier AD7013MT digital desktop microscope. Fig. 16 illustrates images captured by a microscope of four randomly chosen 0.5 mm-diameter apertures. Fig. 17 illustrates images captured by a microscope of four randomly chosen 0.9 mm-diameter apertures from the experimental sample. The mean values for the printed diameters are 0.44 mm and 0.86 mm, respectively, which are both below the intended design specifications. Future work will attempt to calibrate the printing procedure so that initially over-sized holes are printed with the intended diameter.

VII. Numerical models

In this paper numerical models are set-up and solved for both the MP-MPPA-I and MP-MPPA-II designs of Fig. 2 for normal *and* grazing acoustic incidence but *without* flow.

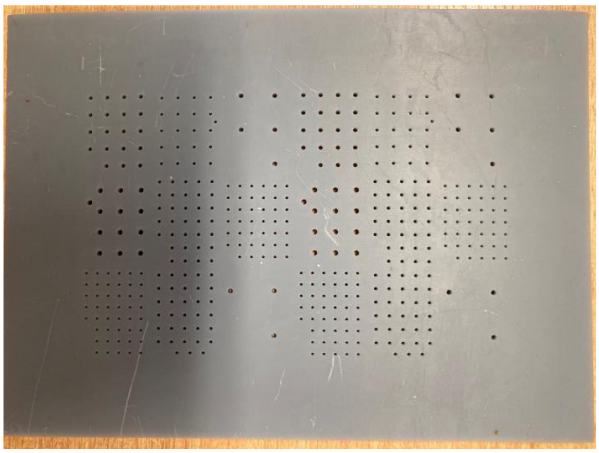

(a) A top-down view of the top MPP (face-plate) of MC-MPPA-II-N 3D printed by MSLA.

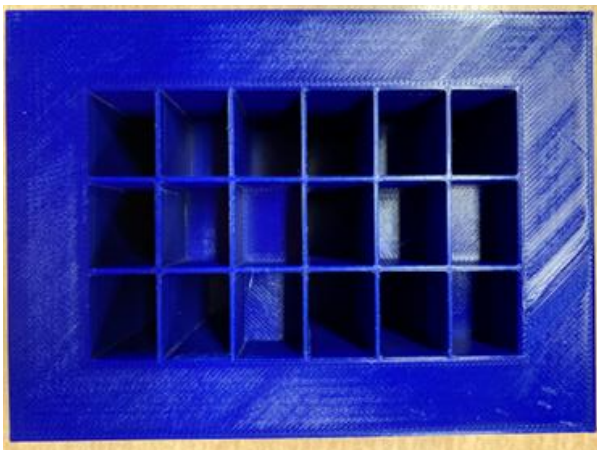

(b) A top-down view of the sub-chambers in MC-MPPA-II-N that exhibit varying depths

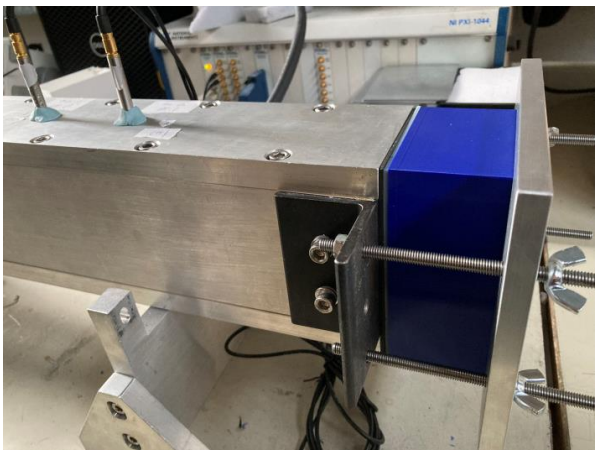

(c) Experimental impedance tube set-up for MC-MPPA-II-N

Fig. 8 Photo images of MC-MPPA-II-N.

A. Under normal acoustic incidence conditions

The sound absorption performance of both MC-MPPA-I-N and MC-MPPA-II-N for normal incident acoustic waves was evaluated numerically using COMSOL 6.0 software. The 3D geometry of the numerical model matched that of the rectangular normal impedance tube depicted in Fig. 6. Further information regarding the numerical simulations of MC-MPPA-I-N can be found in Section 3.3 of Wang and Bennett [16].

B. Under grazing acoustic incidence conditions

In the present investigation, the numerical acoustic grazing rig was generated using the Acoustics Module integrated within the COMSOL Multiphysics software framework. A straight, rectangular duct featuring a cross-sectional dimension of 50 mm in width and 40 mm in height is examined, as depicted in Fig. 9. This geometry is examined as future grazing flow experiments will be performed in the LAUM, Le Mans facility with the same dimensions. The lined section spans a length of 200 mm. Five MC-MPPAs (with dimensions of L = 50 mm and W = 40 mm) are arranged in parallel along the duct in the liner location, resulting in a treatment that is 200 mm long and 50 mm wide, making it a good fit for the dimensions of this duct's experimental section. In order to ensure numerical precision, a criterion was set whereby the maximum size of the unstructured triangular mesh was restricted to a value that is 20 times less than the shortest wavelength of interest, which, for a frequency of 2000 Hz, equates to 0.17/20 m. At the current phase of our investigation, we are not accounting for the influence of grazing flow; that is, our COMSOL model does not incorporate

airflow, or the airflow Mach number can be considered to be zero. The grazing acoustic incidence tube setup involves the introduction of a plane acoustic wave into the system at its upstream end. To simulate this, a pressure wave with an amplitude of 1 Pa, is added as a Background Acoustics Field characteristic in a restricted domain, backed by a perfectly matched layer (PML). This facilitates the exit of reflected waves from the computational domain. To further prevent reflection and ensure the free exit of waves, a PML is also integrated at the downstream outlet.This setting is identical to that in Ref. [49].

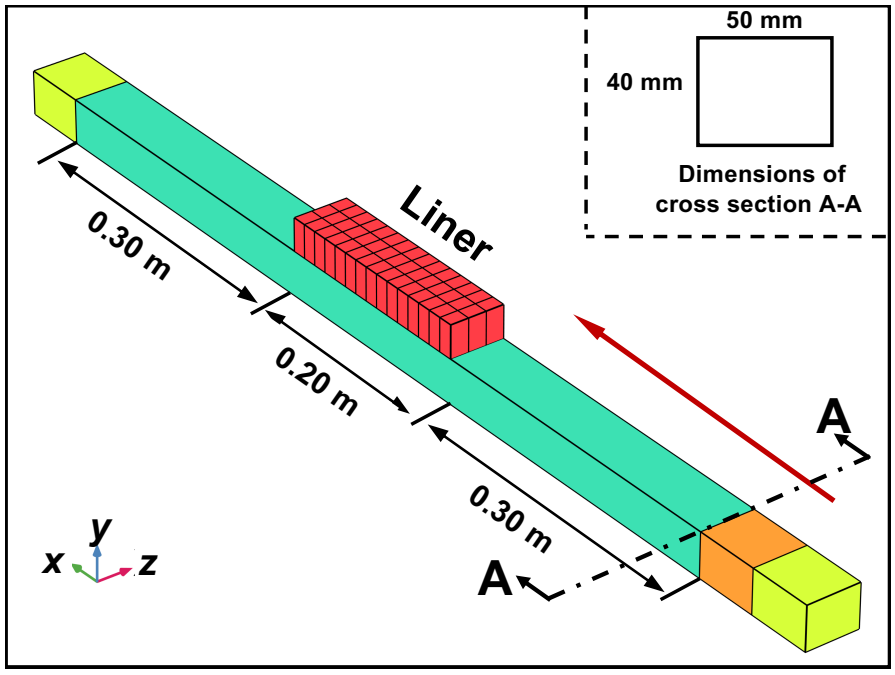

Fig. 9 Sketch of the grazing acoustic incidence tube modeled in COMSOL. Both the MC-MPPA-I and MC-MPPA-II technologies are examined in the liner location. The direction of the incident wave is denoted by the red arrow. The orange domain illustrates the background acoustic field, while the yellow domain signifies the perfectly match layer (PML).

VIII. Results and Discussions

Both technologies: MC-MPPA-I and MC-MPPA-II, were examined in both normal and grazing acoustic impedance conditions without flow.

In normal impedance, the optimized analytical result leads to the design and manufacture of the experimental test-pieces named: MC-MPPA-I-N and MC-MPPA-II-N, and also to the definition of the numerical model. All three sets of results for both technologies are compared to one another for a sub-chamber depth of 20 mm and 50 mm.

In grazing acoustic impedance, MC-MPPA-I and MC-MPPA-II are once again optimized but for a grazing acoustic condition. The performance of both technologies: MC-MPPA-I-G and MC-MPPA-II-G, is examined by way of the Transmission Loss as a function of frequency and a function of the 3D acoustic field in the duct. No experimental results are presented in grazing *flow* currently but such tests are planned for future work.

A. Normal acoustic incidence

Figures 10 and 11 illustrate the theoretical, numerical, and experimental sound absorption curves for MC-MPPA-I-N and MC-MPPA-II-N, respectively, under normal acoustic incidence conditions in the frequency range of [200 2000] Hz.

1. Acoustic performance of MC-MPPA-I-N

According to Fig. 10, the overall sound absorption coefficient of MC-MPPA-I-N for normal incident sound waves was examined within the frequency range of 200 Hz to 2000 Hz. The results of analytical, numerical and experimental analyses show that the coefficient values are 0.6746, 0.6686, and 0.6703, respectively. It is worth noting that the performance of MC-MPPA-I-N is exceptional when the frequency exceeds 660 Hz, with analytical analysis yielding c_α = 0.8586, numerical analysis yielding c_α = 0.8428, and experimental analysis yielding c_α = 0.8273.

It is worth noting that the sub-chamber depth within the MC-MPPA-I-N is only 20mm. Experimental results show that an absorption coefficient of approximately 0.80 was obtained at 780 Hz when the air cavity depth was 20 mm, corresponding to a depth-to-wavelength ratio of 22. In the acoustic metamaterial literature this would be termed a deeply sub-wavelength absorber. Moreover, the analytical, numerical, and experimental results exhibit a high degree of agreement.

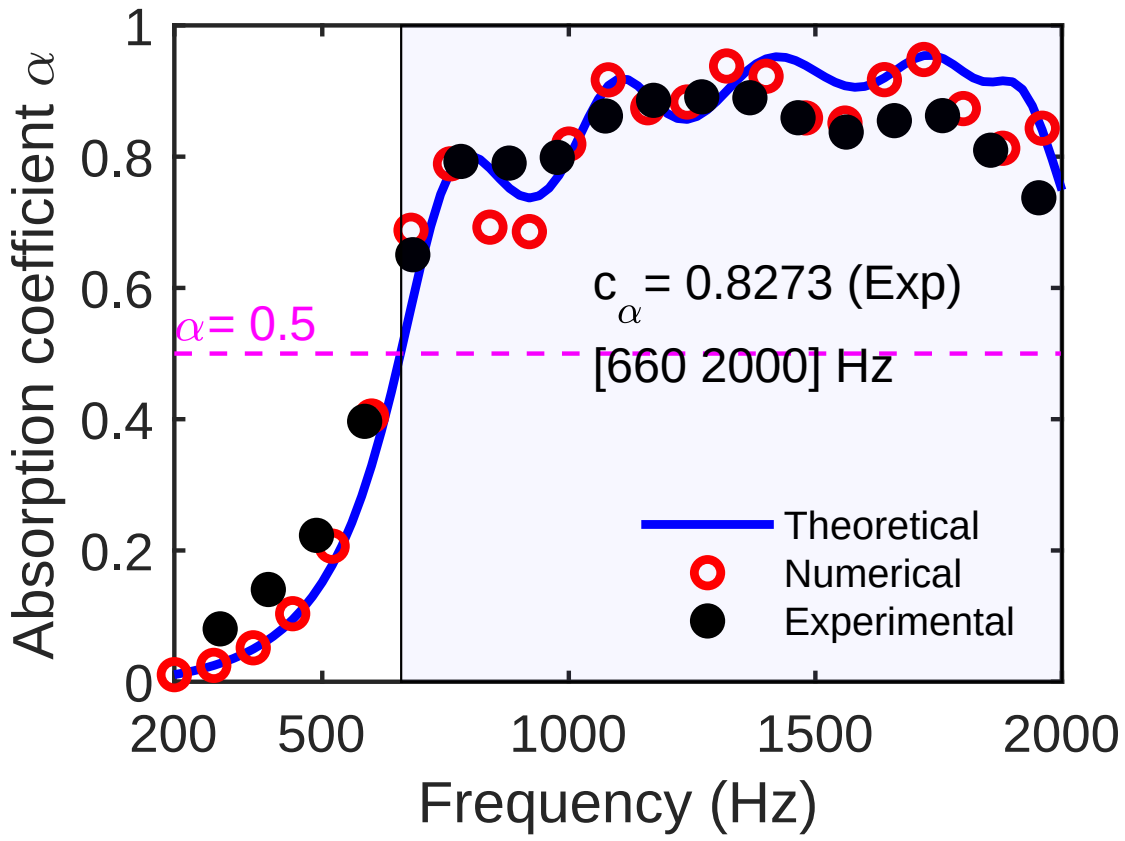

Fig. 10 The analytical (TpIM), numerical and experimental sound absorption coefficients for test sample MC-MPPA-I-N under normal acoustic incidence [16]. D=20 mm. The blue region represents the frequency range of [660 2000] Hz, within which the experimental c_α is measured to be 0.8273.

2. Acoustic performance of MC-MPPA-II-N

In the case of MC-MPPA-II-N, the air sub-cavities' depths are not uniform, see Fig. 8. The test-piece evaluated in this study has a maximum depth of 50 mm for its air sub-chambers (refer to Table 4). Fig. 11 shows that the overall sound absorption coefficient of MC-MPPA-II-N for normal incident sound waves, as determined through analytical, numerical, and experimental analyses, is 0.7882, 0.7718, and 0.7609, respectively, within the studied frequency range of 200 Hz to 2000 Hz. It is worth noting that MC-MPPA-II-N exhibits exceptional performance at frequencies greater than 400 Hz, with analytical analysis yielding c_α = 0.8671, numerical analysis yielding c_α = 0.8485, and experimental analysis yielding c_α = 0.8284. Moreover, the analytical, numerical, and experimental results exhibit a high degree of agreement.

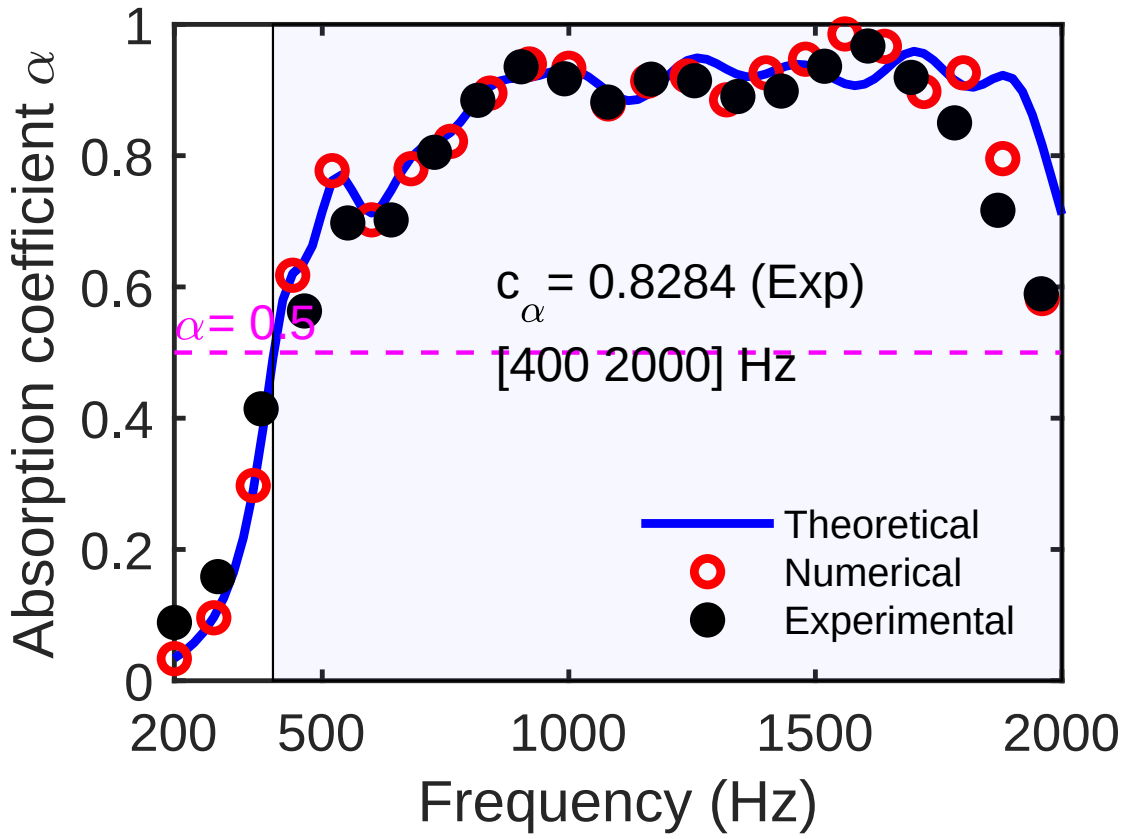

Fig. 11 The analytical (TpIM), numerical and experimental sound absorption coefficients for test sample MC-MPPA-II-N under normal acoustic incidence. The blue region represents the frequency range of [400 2000] Hz, within which the experimental c_α is measured to be 0.8284.

B. Grazing acoustic incidence

Figs. 12 and 13 show the optimized transmission loss curves for MC-MPPA-I-G and MC-MPPA-II-N, respectively, with three different sub-chamber depths (10 mm, 30 mm, and 50 mm) under grazing acoustic incidence conditions in frequency range of [600 2000] Hz, after implementing the optimization strategy outlined in Section V.B. To obtain a clearer understanding of the noise attenuation performance, the acoustic pressure fields at 800 Hz, 1200 Hz, and 1600 Hz for $M = 0$ are shown in Figs. 14 and 15 as a function of depth.

1. Acoustic performance of MC-MPPA-I-G

Concerning the acoustic performance of MC-MPPA-I-G under grazing incidence conditions, it can be seen in Fig. 12 that the optimized design results in very high transmission loss. The numerical transmission loss peak for MC-MPPA-I-G with a sub-chamber depth of 10 mm reaches 46 dB at 1520 Hz, and the numerical transmission loss surpasses 10 dB in the frequency range of [1360, 1700] Hz (as shown in blue region in Fig. 12). For a sub-chamber depth of 30 mm, the peak reaches 66 dB at 1180 Hz, and the transmission loss exceeds 10 dB in the frequency range of [980, 1540] Hz (as shown in red region in Fig. 12). Lastly, with a sub-chamber depth of 50 mm, the peak attains 55 dB at 880 Hz, and the transmission loss surpasses 10 dB in the frequency range of [700, 1260] Hz (as shown in black region in Fig. 12).

2. Acoustic performance of MC-MPPA-II-G

In terms of the acoustic performance of MC-MPPA-II-G under grazing incidence conditions, MC-MPPA-II-G displays lower peak TL but more broadband sound absorption characteristics. As illustrated in Fig. 13, the numerical transmission loss of MC-MPPA-II with a sub-chamber depth of 10 mm exceeds 10 dB in the frequency range of

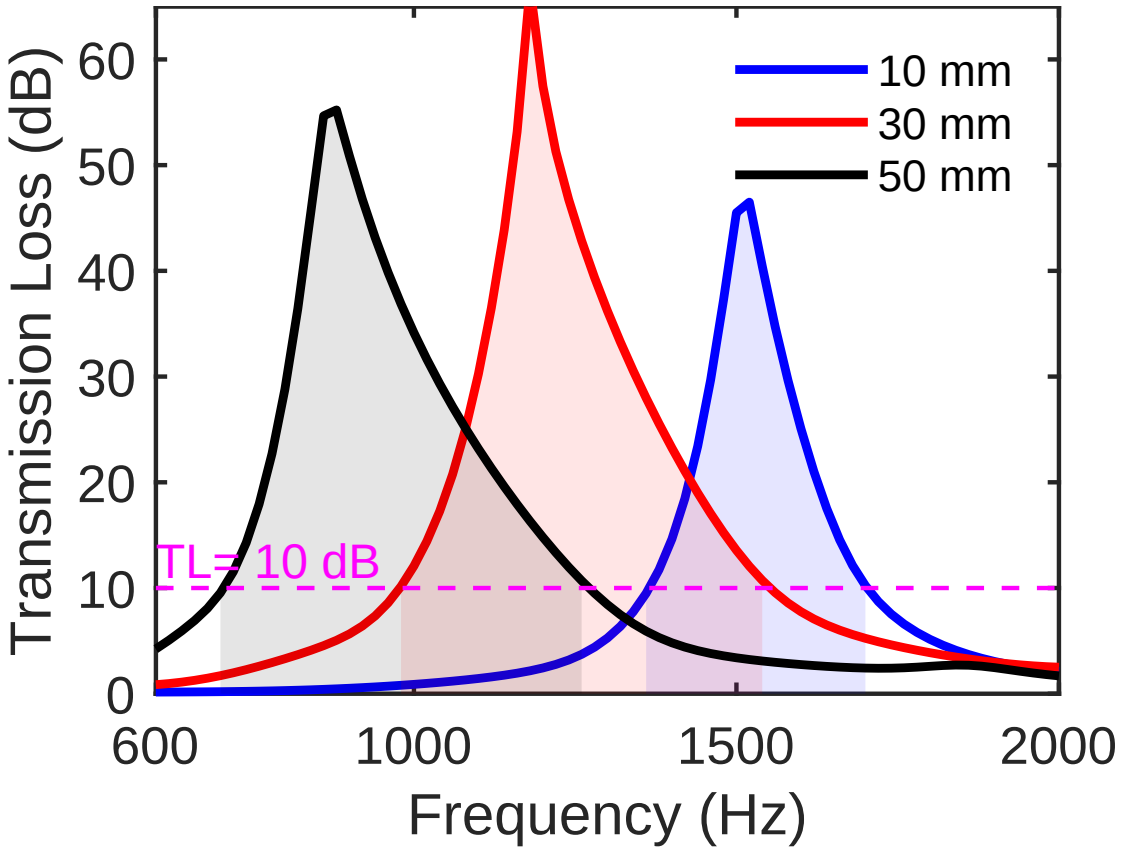

Fig. 12 Optimized sound transmission loss (in dB) of the MC-MPPA-I-G test sample under grazing acoustic incidence in the absence of flow.

[1280, 1800] Hz (as shown in blue region in Fig. 13) . Similarly, for a sub-chamber depth of 30 mm, the numerical transmission loss surpasses 10 dB in the frequency range of [1000, 1740] Hz (as shown in red region in Fig. 13), and for a sub-chamber depth of 50 mm, it surpasses 10 dB in the frequency range of [820, 1700] Hz (as shown in black region in Fig. 13).

3. The effect of sub-chamber's air cavity depth

For MC-MPPA-I-G under grazing incidence conditions, as depicted in Fig. 12, the sound transmission loss peak's location is a function of the sub-chamber depth. As would be expected, when the sub-chamber depth increases from 10 mm to 50 mm, the sound transmission loss peak shifts to a lower frequency. For MC-MPPA-II-G, however, under grazing incidence conditions, as illustrated in Fig. 13, the sound transmission loss is less dominated by a single peak. However, the transmission loss bandwidth is dependent on the sub-chamber depth. As the sub-chamber depth increases from 10 mm to 50 mm, the sound transmission loss bandwidth not only expands but also shifts to a lower frequency.

The acoustic pressure fields of MC-MPPA-I-G and MC-MPPA-II-G at 800 Hz, 1200 Hz, and 1600 Hz for a Mach number of 0 are presented in Figs. 12 and 13. For MC-MPPA-I-G, the downstream sound pressure intensity significantly diminishes at various frequencies depending on the sub-chamber depth. With a sub-chamber depth of 10 mm, the intensity decreases notably at around 1600 Hz. At a sub-chamber depth of 30 mm, the intensity diminishes significantly at approximately 1200 Hz. Similarly, with a sub-chamber depth of 50 mm, the downstream sound pressure substantially reduces at around 800 Hz.

For MC-MPPA-II-G, with a sub-chamber depth of 10 mm, the downstream sound pressure weakens notably not only at 1600 Hz but also at around 1200 Hz. At a sub-chamber depth of 30 mm, the downstream sound pressure intensity significantly reduces between 1200 Hz and 1600 Hz. Lastly, with a sub-chamber depth of 50 mm, the downstream sound pressure intensity considerably decreases not only between 1200 Hz and 1600 Hz but also around 800 Hz.

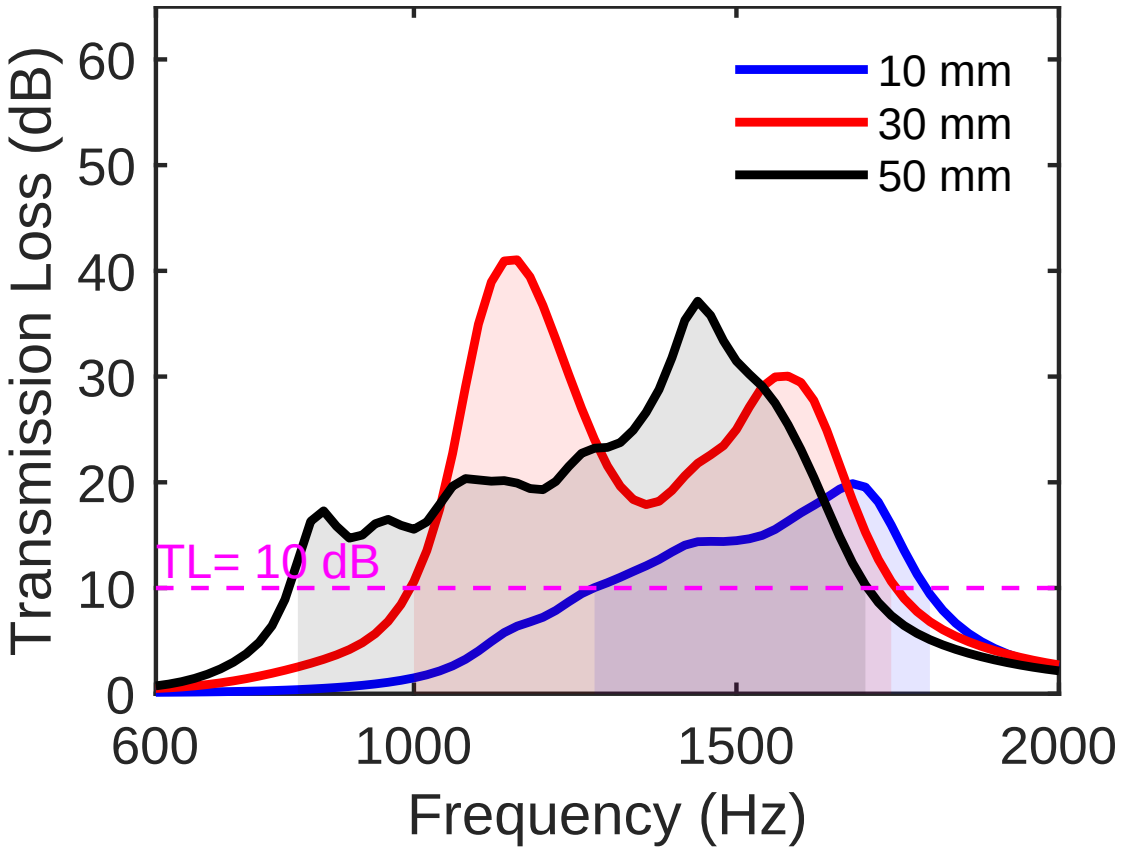

Fig. 13 Optimized sound transmission loss (in dB) of the MC-MPPA-II-G under grazing acoustic incidence in the absence of flow.

The optimized acoustic performance of MC-MPPA-I-G and MC-MPPA-II-G demonstrates significant differences under grazing incidence conditions, which can be attributed to the potential variability in MC-MPPA-II-G's sub-chamber depths, allowing depth variations in individual sub-cavities. As a result, this leads to an increased number of resonances and a broader bandwidth for transmission losses. In contrast, the current study reveals that MC-MPPA-I-G requires uniform sub-chamber depths, yielding fewer resonances than MC-MPPA-II-G. Nevertheless, this results in a more pronounced transmission loss peak for MC-MPPA-I-G compared to MC-MPPA-II-G.

IX. Conclusions and Future work

In this study, we design and optimize two distinct types of MC-MPPA for normal incidence sound absorption and grazing incidence noise absorption, employing the two-point impedance method and Cremer impedance, the latter of which allows or optimization in grazing conditions. The main conclusions of this paper are as follows:

(1) Both MC-MPPA-I and MC-MPPA-II offer broadband and low-frequency sound absorption under normal incidence conditions. For MC-MPPA-I-N, the experimental overall absorption coefficient (c_α) is measured to be 0.8273 in the frequency range of [660, 2000] Hz when its depth is 20 mm. For MC-MPPA-II-N, the experimental overall absorption coefficient (c_α) is measured to be 0.8284 in the frequency range of [400, 2000] Hz when its maximum depth is 50 mm.

(2) Both MC-MPPA-I and MC-MPPA-II can function as deeply sub-wavelength broadband noise absorbers. Experimental results for MC-MPPA-I-N demonstrate an absorption coefficient of approximately 0.80 at 780 Hz with an air cavity depth of 20 mm, corresponding to a depth-to-wavelength ratio of 22. Similarly, for MC-MPPA-II-N, experimental results indicate an absorption coefficient of approximately 0.80 at 725 Hz with an air cavity depth of 50 mm, corresponding to a depth-to-wavelength ratio of 9.

(3) The integration of the two-point impedance method, a model for an MPP in grazing acoustic conditions and

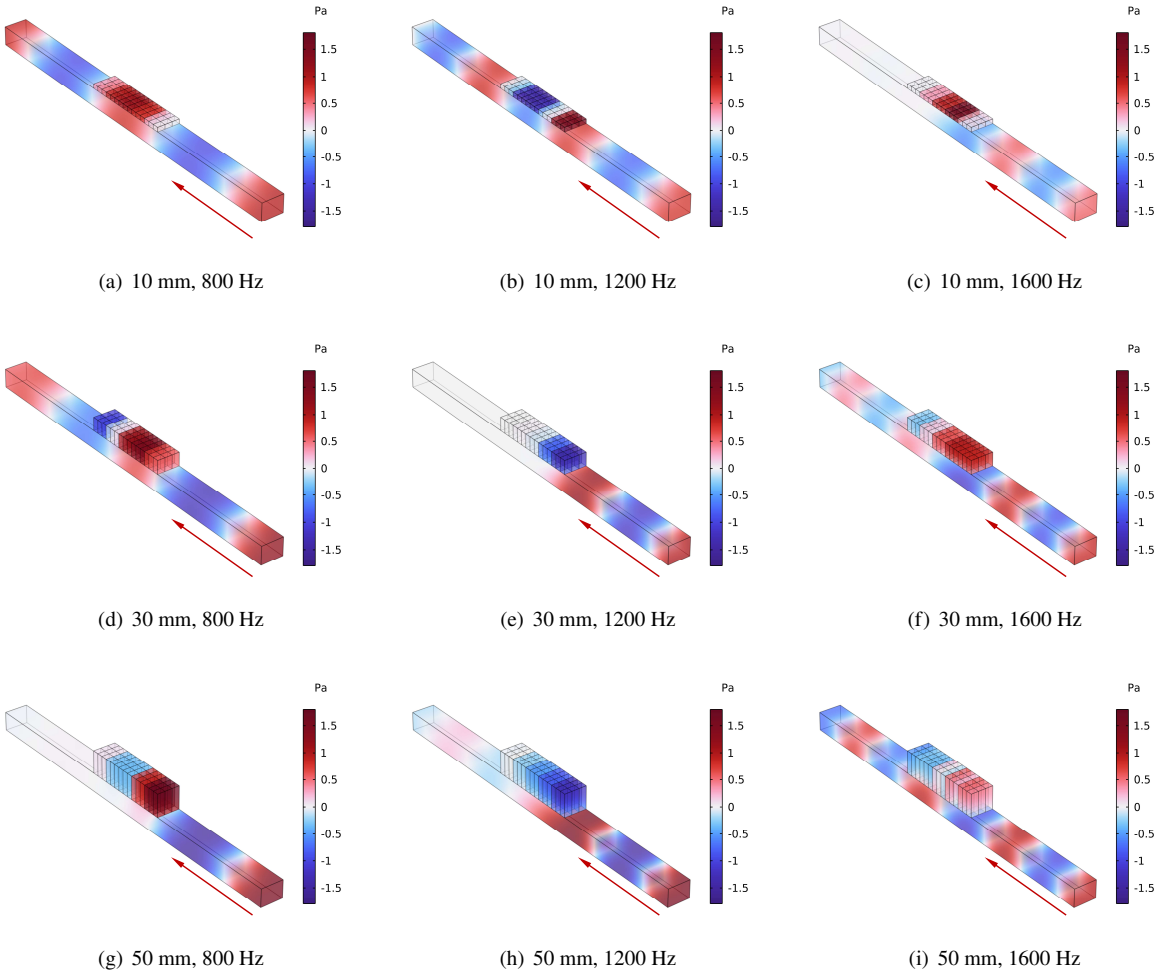

(a) 10 mm, 800 Hz (b) 10 mm, 1200 Hz (c) 10 mm, 1600 Hz

(d) 30 mm, 800 Hz (e) 30 mm, 1200 Hz (f) 30 mm, 1600 Hz

(g) 50 mm, 800 Hz (h) 50 mm, 1200 Hz (i) 50 mm, 1600 Hz

Fig. 14 Acoustic pressure fields of MC-MPPA-I-G and the grazing tube at frequencies of 800, 1200, and 1600 Hz in the absence of flow. The direction of the incident wave is indicated by the red arrow.

the Cremer impedance enables the design and optimization of an MC-MPPA for grazing acoustic conditions. Additionally, we propose a novel cost function for MC-MPPA optimization under grazing flow or acoustic incidence conditions, facilitating the identification of the optimum MC-MPPA design across an extensive frequency range.

(4) Both MC-MPPA-I and MC-MPPA-II offer optimal acoustic performance under grazing acoustic incidence conditions. With a sub-chamber depth of merely 10 mm, MC-MPPA-I achieves a transmission loss of 46 dB at 1520 Hz. For MC-MPPA-II, a sub-chamber depth of 50 mm results in a transmission loss exceeding 10 dB in the frequency range of [820, 1700] Hz.

(5) When MC-MPPA under grazing incidence conditions, both the location of the sound transmission loss peak and the bandwidth are highly sensitive to sub-chamber depth. Notably, varying sub-chamber depths can result in a higher number of resonances and an expanded bandwidth for sound transmission losses.

We will subsequently conduct experiments to validate the acoustic performance of MC-MPPA under grazing flow conditions. The influence of flow and flow speed on MC-MPPA's acoustic behavior will be assessed in these conditions. Additionally, we will modify the sound level amplitude to investigate potential non-linearity. The Acoustics Laboratory of Le Mans University (LAUM) houses a state-of-the-art experimental grazing flow rig, representative of aeroengines and telecommunications servers found in data centers, for instance. This uniform rectangular duct has an internal 50 × 40 mm cross-section. A compressor generates a mean flow within this duct, with an adjustable flow rate up to a mean velocity of Mach 0.25 [50]. The optimized MC-MPPA will be placed in the wall of a 200mm-long test section. Impedance eduction will enable the measurement of liner impedance evolution as a function of flow velocity, and the

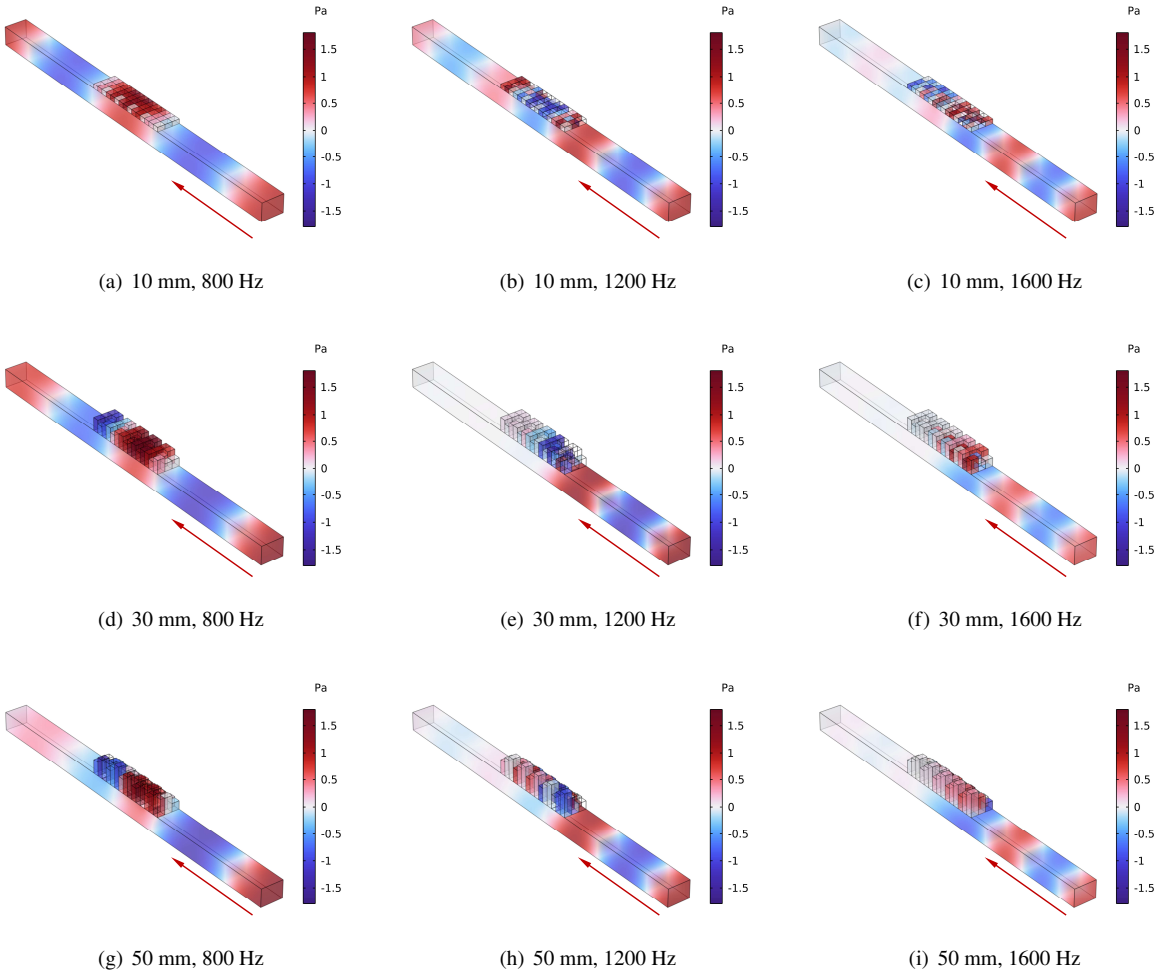

(a) 10 mm, 800 Hz (b) 10 mm, 1200 Hz (c) 10 mm, 1600 Hz

(d) 30 mm, 800 Hz (e) 30 mm, 1200 Hz (f) 30 mm, 1600 Hz

(g) 50 mm, 800 Hz (h) 50 mm, 1200 Hz (i) 50 mm, 1600 Hz

Fig. 15 Acoustic pressure fields of MC-MPPA-II-G and the grazing tube at frequencies of 800, 1200, and 1600 Hz in the absence of flow. The direction of the incident wave is indicated by the red arrow.

model for flow effects will be assessed against these measurements.

Appendix

A. Geometric parameters of test sample in the experimental validation

Perforation diameter (mm)									
$d_{t(1,1)}$	0.98	$d_{t(1,2)}$	0.63	$d_{t(1,3)}$	0.64	$d_{t(2,1)}$	0.90	$d_{t(2,2)}$	0
$d_{t(2,3)}$	0	$d_{t(3,1)}$	0	$d_{t(3,2)}$	0.50	$d_{t(3,3)}$	0.50		
$d_{i(1)}$	0.50	$d_{i(2)}$	0.50	$d_{i(3)}$	0	$d_{i(4)}$	0.50	$d_{i(5)}$	0.50
$d_{i(6)}$	0	$d_{i(7)}$	1.00	$d_{i(8)}$	0	$d_{i(9)}$	0	$d_{i(10)}$	0.50
$d_{i(11)}$	0	$d_{i(12)}$	0.51						
Perforation porosity (%)									
$\varphi_{t(1,1)}$	5.00	$\varphi_{t(1,2)}$	5.00	$\varphi_{t(1,3)}$	5.00	$\varphi_{t(2,1)}$	5.00	$\varphi_{t(2,2)}$	0
$\varphi_{t(2,3)}$	0	$\varphi_{t(3,1)}$	0	$\varphi_{t(3,2)}$	4.22	$\varphi_{t(3,3)}$	4.22		
$\varphi_{i(1)}$	5.00	$\varphi_{i(2)}$	5.00	$\varphi_{i(3)}$	0	$\varphi_{i(4)}$	0.58	$\varphi_{i(5)}$	1.47
$\varphi_{i(6)}$	0	$\varphi_{i(7)}$	1.28	$\varphi_{i(8)}$	0	$\varphi_{i(9)}$	0	$\varphi_{i(10)}$	5.00
$\varphi_{i(11)}$	0	$\varphi_{i(12)}$	5.00						
perforation number									
$n_{t(1,1)}$	13	$n_{t(1,2)}$	32	$n_{t(1,3)}$	31	$n_{t(2,1)}$	16	$\varphi_{t(2,2)}$	0
$n_{t(2,3)}$	0	$n_{t(3,1)}$	0	$n_{t(3,2)}$	43	$n_{t(3,3)}$	43		
$n_{i(1)}$	64	$n_{i(2)}$	64	$n_{i(3)}$	0	$n_{i(4)}$	10	$n_{i(5)}$	24
$n_{i(6)}$	0	$n_{i(7)}$	4	$n_{i(8)}$	0	$n_{i(9)}$	0	$n_{i(10)}$	81
$n_{i(11)}$	0	$n_{i(12)}$	61						
Other geometric parameters									
L	50 mm	W	40 mm	D	20 mm	τ_i	1 mm	τ_t	2 mm

Table 3 Geometric parameters of the MC-MPPA-I-N.

Perforation diameter (mm)									
$d_{t(1,1)}$	0.90	$d_{t(1,2)}$	0.53	$d_{t(1,3)}$	0.90	$d_{t(2,1)}$	0.62	$d_{t(2,2)}$	0.62
$d_{t(2,3)}$	0.58	$d_{t(3,1)}$	0.52	$d_{t(3,2)}$	0.99	$d_{t(3,3)}$	0.82		
Perforation porosity (%)									
$\varphi_{t(1,1)}$	0.95	$\varphi_{t(1,2)}$	4.45	$\varphi_{t(1,3)}$	1.59	$\varphi_{t(2,1)}$	5.00	$\varphi_{t(2,2)}$	5.02
$\varphi_{t(2,3)}$	2.77	$\varphi_{t(3,1)}$	4.87	$\varphi_{t(3,2)}$	4.97	$\varphi_{t(3,3)}$	5.01		
perforation number									
$n_{t(1,1)}$	3	$n_{t(1,2)}$	41	$n_{t(1,3)}$	5	$n_{t(2,1)}$	33	$\varphi_{t(2,2)}$	33
$n_{t(2,3)}$	21	$n_{t(3,1)}$	45	$n_{t(3,2)}$	13	$n_{t(3,3)}$	19		
Air cavity depth (mm)									
$D_{t(1,1)}$	50.00	$D_{t(1,2)}$	50.00	$D_{t(1,3)}$	50.00	$D_{t(2,1)}$	28.30	$\varphi_{t(2,2)}$	21.43
$D_{t(2,3)}$	50.00	$D_{t(3,1)}$	40.07	$D_{t(3,2)}$	13.14	$n_{t(3,3)}$	16.32		
Other geometric parameters									
L	50 mm	W	40 mm	D	50 mm	τ_i	1 mm	τ_t	2 mm

Table 4 Geometric parameters of the MC-MPPA-II-N.

B. Microscope images of 0.5 mm-diameter and 0.9 mm-diameter 3D-printed holes from the test sample

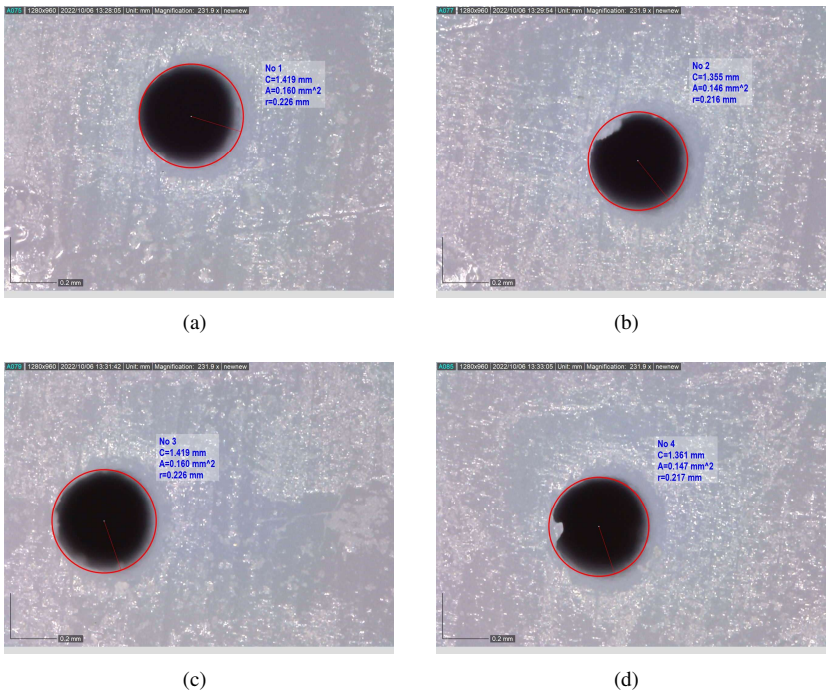

(a) (b)

(c) (d)

Fig. 16 Microscope images of four arbitrary 0.5 mm-diameter MSLA 3D-printed holes from test samples, where r represents the radius of the hole, A represents the area of the hole, and C represents the perimeter of the hole.

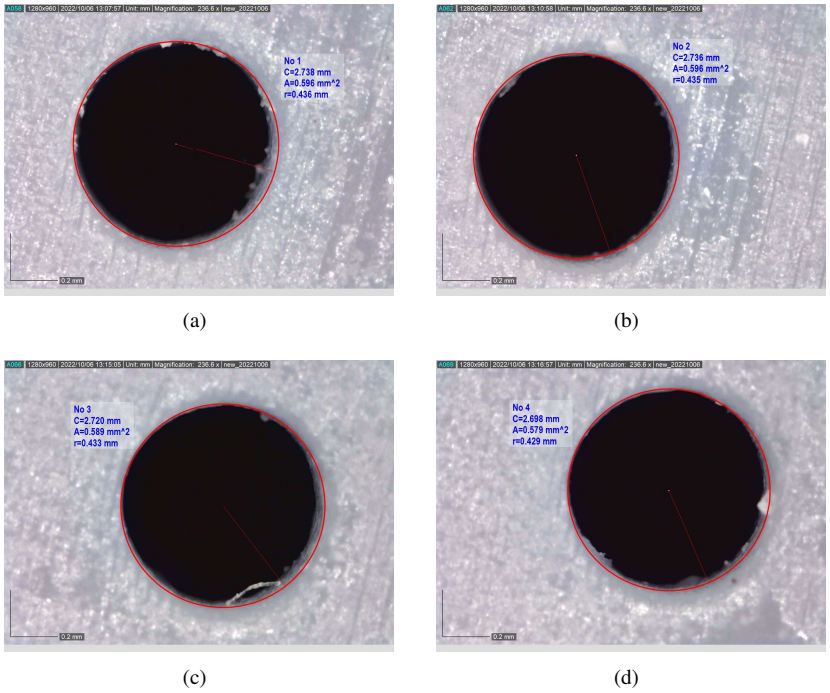

(a) (b)

(c) (d)

Fig. 17 Microscope images of four arbitrary 0.9 mm-diameter MSLA 3D-printed holes from test samples, where r represents the radius of the hole, A represents the area of the hole, and C represents the perimeter of the hole.

References

[1] Morrell, S., Taylor, R., and Lyle, D., "A Review of Health Effects of Aircraft Noise," *Australian and New Zealand Journal of Public Health*, Vol. 21, No. 2, 1997, pp. 221–236. https://doi.org/10.1111/j.1467-842X.1997.tb01690.x.

[2] Nassur, A.-M., Léger, D., Lefèvre, M., Elbaz, M., Mietlicki, F., Nguyen, P., Ribeiro, C., Sineau, M., Laumon, B., and Evrard, A.-S., "Effects of Aircraft Noise Exposure on Heart Rate during Sleep in the Population Living Near Airports," *International Journal of Environmental Research and Public Health*, Vol. 16, No. 2, 2019. https://doi.org/10.3390/ijerph16020269.

[3] Basner, M., Samel, A., and Isermann, U., "Aircraft Noise Effects on Sleep: Application of the Results of a Large Polysomnographic Field Study," *The Journal of the Acoustical Society of America*, Vol. 119, No. 5, 2006, pp. 2772–2784. https://doi.org/10.1121/1.2184247.

[4] Mahashabde, A., Wolfe, P., Ashok, A., Dorbian, C., He, Q., Fan, A., Lukachko, S., Mozdzanowska, A., Wollersheim, C., Barrett, S. R. H., Locke, M., and Waitz, I. A., "Assessing the Environmental Impacts of Aircraft Noise and Emissions," *Progress in Aerospace Sciences*, Vol. 47, No. 1, 2011, pp. 15–52. https://doi.org/10.1016/j.paerosci.2010.04.003.

[5] Astley, R. J., A. Agarwal, K. R. Holland, P. F. Joseph, R. Sugimoto, R. H. Self, M. G. Smith, and B. J. Tester, "Predicting and Reducing Aircraft Noise," *14th International Congress on Sound and Vibration (ICSV14)*, Cairns, Australia, 2007, p. 819.

[6] Wang, J., and Ma, W., "Deconvolution Algorithms of Phased Microphone Arrays for the Mapping of Acoustic Sources in an Airframe Test," *Applied Acoustics*, Vol. 164, 2020, p. 107283. https://doi.org/10.1016/j.apacoust.2020.107283.

[7] Wang, J., and Ma, W., "Comparison of Deconvolution Algorithms of Phased Microphone Array for Sound Source Localization in an Airframe Noise Test," *Proceedings of the International Conference on Aerospace System Science and Engineering 2019*, Springer Singapore, 2019, pp. 81–90. https://doi.org/10.1007/978-981-15-1773-0_7.

[8] Baudin, C., Lefèvre, M., Champelovier, P., Lambert, J., Laumon, B., and Evrard, A.-S., "Aircraft Noise and Psychological Ill-Health: The Results of a Cross-Sectional Study in France," *International Journal of Environmental Research and Public Health*, Vol. 15, No. 8, 2018. https://doi.org/10.3390/ijerph15081642.

[9] Torija, A. J., and Clark, C., "A Psychoacoustic Approach to Building Knowledge about Human Response to Noise of Unmanned Aerial Vehicles," *International Journal of Environmental Research and Public Health*, Vol. 18, No. 2, 2021. https://doi.org/10.3390/ijerph18020682.

[10] Zaporozhets, O., "Balanced Approach to Aircraft Noise Management," *Aviation Noise Impact Management: Technologies, Regulations, and Societal Well-being in Europe*, Springer International Publishing, 2022, pp. 29–56. https://doi.org/10.1007/978-3-030-91194-2_3.

[11] Astley, R. J., "Can Technology Deliver Acceptable Levels of Aircraft Noise?" *INTER-NOISE and NOISE-CON Congress and Conference Proceedings*, 5, Vol. 249, Institute of Noise Control Engineering, 2014, pp. 2622–2633.

[12] Maa, D.-Y., "Theory and Design of Microperforated Panel Sound-absorbing Constructions," *Scientia Sinica*, Vol. 18, 1975, pp. 55–71. https://doi.org/10.1360/ya1975-18-1-55.

[13] Maa, D.-Y., "Microperforated-Panel Wideband Absorbers," *Noise Control Engineering Journal*, Vol. 29, 1987, pp. 77–84. https://doi.org/10.3397/1.2827694.

[14] Maa, D.-Y., "Potential of Microperforated Panel Absorber," *The Journal of the Acoustical Society of America*, Vol. 104, No. 5, 1998, pp. 2861–2866. https://doi.org/https://doi.org/10.1121/1.423870.

[15] McKay, A., Davis, I., Killeen, J., and Bennett, G. J., "SeMSA: a Compact Super Absorber Optimised for Broadband, Low-frequency Noise Attenuation," *Scientific Reports*, Vol. 10, No. 1, 2020, p. 17967. https://doi.org/10.1038/s41598-020-73933-0.

[16] Wang, J., and Bennett, G. J., "Multi-chamber Micro-perforated Panel Absorbers Optimised for High Amplitude Broadband Absorption Using a Two-point Impedance Method," *Journal of Sound and Vibration*, Vol. 547, 2023, p. 117527. https://doi.org/10.1016/j.jsv.2022.117527.

[17] Davis, I., McKay, A., and Bennett, G. J., "A Graph-theory Approach to Optimisation of an Acoustic Absorber Targeting a Specific Noise Spectrum that Approaches the Causal Optimum Minimum Depth," *Journal of Sound and Vibration*, Vol. 505, 2021, p. 116135. https://doi.org/10.1016/j.jsv.2021.116135.

[18] Killeen, J., Davis, I., Wang, J., and Bennett, G. J., "Fan-noise Reduction of Data Centre Telecommunications' Server Racks, with an Acoustic Metamaterial Broadband, Low-frequency Sound-absorbing Liner," *Applied Acoustics*, Vol. 203, 2023, p. 109229. https://doi.org/10.1016/j.apacoust.2023.109229.

[19] Rice, E. J., "Theoretical Study of the Acoustic Impedance of Orifices in the Presence of a Steady Grazing Flow," *The Journal of the Acoustical Society of America*, Vol. 59, No. S1, 1976, pp. S32–S32. https://doi.org/10.1121/1.2002637.

[20] Rogers, T., and Hersh, A., "The Effect of Grazing Flow on the Steady State Resistance of Square-edged Orifices," *2nd Aeroacoustics Conference*, 1975. https://doi.org/10.2514/6.1975-493.

[21] Hersh, A., Walker, B., and Bucka, M., "Effect of Grazing Flow on the Acoustic Impedance of Helmholtz Resonators Consisting of Single and Clustered Orifices," *11th Fluid and PlasmaDynamics Conference*, 1978. https://doi.org/10.2514/6.1978-1124.

[22] Guo, Y., Allam, S., and Åbom, M., "Micro-Perforated Plates for Vehicle Applications," *37th International Congress and Exposition on Noise Control Engineering*, 2008.

[23] Åbom, M., and Allam, S., "Dissipative Silencers Based on Micro-perforated Plates," *SAE Technical Paper, 2013-24-0071*, 2013. https://doi.org/10.4271/2013-24-0071.

[24] Allam, S., and Åbom, M., "A New Type of Muffler Based on Microperforated Tubes," *Journal of Vibration and Acoustics*, Vol. 133, No. 3, 2011. https://doi.org/10.1115/1.4002956.

[25] Zhang, X., and Cheng, L., "Acoustic Impedance of Micro-perforated Panels in a Grazing Flow," *The Journal of the Acoustical Society of America*, Vol. 145, 2019, p. 2461. https://doi.org/10.1121/1.5098785.

[26] Zhang, X., Yang, C., Cheng, L., and Zhang, P., "An Experimental Investigation on the Acoustic Properties of Micro-perforated Panels in a Grazing Flow," *Applied Acoustics*, Vol. 159, 2020. https://doi.org/10.1016/J.APACOUST.2019.107119.

[27] Wu, G., Guan, Y. H., Ji, C., and Gay, F. Y. X., "Experimental Studies on Sound Absorption Coefficients of Perforated Pipes with Bias-grazing Flows at Low Mach and Strouhal Number," *Aerospace Science and Technology*, Vol. 107, 2020, p. 106255. https://doi.org/10.1016/j.ast.2020.106255.

[28] Jones, M., Watson, W., Nark, D., Howerton, B., and Brown, M., "A Review of Acoustic Liner Experimental Characterization at NASA Langley," Tech. rep., NASA Langley Research Center, Hampton, Virginia 23681-2199, 2020. https://doi.org/10.13140/RG.2.2.15613.10720.

[29] Jones, M., Howerton, B., and Ayle, E., "Evaluation of Parallel-Element, Variable-Impedance, Broadband Acoustic Liner Concepts," *18th AIAA/CEAS Aeroacoustics Conference (33rd AIAA Aeroacoustics Conference)*, 2012. https://doi.org/10.2514/6.2012-2194.

[30] Ma, X., and Su, Z., "Development of Acoustic Liner in Aero Engine: A Review," *Science China Technological Sciences*, Vol. 63, No. 12, 2020, pp. 2491–2504. https://doi.org/10.1007/s11431-019-1501-3.

[31] Bake, F., and Knobloch, K., "Novel Liner Concepts," *CEAS Aeronautical Journal*, Vol. 10, No. 1, 2019, pp. 123–136. https://doi.org/10.1007/s13272-019-00380-7.

[32] Jones, M. G., Nark, D. M., Baca, A., and Smith, C. R., "Applications of Parallel-Element, Embedded Mesh-Cap Acoustic Liner Concepts," *2018 AIAA/CEAS Aeroacoustics Conference*, 2018. https://doi.org/10.2514/6.2018-3445.

[33] Wu, F. Y., "Theory of Resistor Networks: the Two-point Resistance," *Journal of Physics A: Mathematical and General*, Vol. 37, No. 26, 2004, pp. 6653–6673. https://doi.org/10.1088/0305-4470/37/26/004.

[34] Tzeng, W. J., and Wu, F. Y., "Theory of Impedance Networks: the Two-point Impedance and LC Resonances," *Journal of Physics A: Mathematical and General*, Vol. 39, No. 27, 2006, pp. 8579–8591. https://doi.org/10.1088/0305-4470/39/27/002.

[35] Cremer, L., "Theory Regarding the Attenuation of Sound Transmitted by Air in a Rectangular Duct with an Absorbing Wall, and the Maximum Attenuation Constant Produced During This Process," *Acustica*, Vol. 3, 1953, pp. 249–263.

[36] Zhang, Z., Bodén, H., and Åbom, M., "The Cremer Impedance: An Investigation of the Low Frequency Behavior," *Journal of Sound and Vibration*, Vol. 459, 2019, p. 114844. https://doi.org/10.1016/j.jsv.2019.07.010.

[37] Zhang, Z., Kabral, R., Nilsson, B., and Åbom, M., "Revisiting the Cremer impedance," *Proceedings of Meetings on Acoustics*, Vol. 30, No. 1, 2017, p. 040009. https://doi.org/10.1121/2.0000619.

[38] Åbom, M., and Jacob, S., "A Comment on the Correct Boundary Conditions for the Cremer Impedance," *JASA Express Letters*, Vol. 1, No. 2, 2021, p. 022801. https://doi.org/10.1121/10.0003546.

[39] Zhang, Z., Åbom, M., Boden, H., Jing, X., and Du, L., "Recent Development in the Cremer Impedance: Experimental Analysis, Numerical Validation and Triple Roots," *25th AIAA/CEAS Aeroacoustics Conference*, 2019. https://doi.org/10.2514/6.2019-2467.

[40] Tester, B., "The Propagation and Attenuation of Sound in Lined Ducts Containing Uniform or "Plug" Flow," *Journal of Sound and Vibration*, Vol. 28, No. 2, 1973, pp. 151–203. https://doi.org/10.1016/S0022-460X(73)80102-6.

[41] Kabral, R., Du, L., Åbom, M., and Knutsson, M., "A Compact Silencer for the Control of Compressor Noise," *SAE International Journal of Engines*, Vol. 7, No. 3, 2014, pp. 1572–1578. https://doi.org/10.4271/2014-01-2060.

[42] Du, L., and Åbom, M., "Using Micro-Perforated Plates to Realize a Silencer Based on the Cremer Impedance," *Proceedings of Forum Acusticum*, 2014.

[43] Zhang, Z., Tiikoja, H., Peerlings, L., and Abom, M., "Experimental Analysis on the 'Exact' Cremer Impedance in Rectangular Ducts," *10th International Styrian Noise, Vibration and Harshness Congress: The European Automotive Noise Conference*, 2018. https://doi.org/10.4271/2018-01-1523.

[44] Spillere, A. M., Braga, D. S., Seki, L. A., Bonomo, L. A., Cordioli, J. A., Bernardo M Rocamora, J., Paulo C Greco, J., dos Reis, D. C., and Coelho, E. L., "Design of a Single Degree of Freedom Acoustic Liner for a Fan Noise Test Rig," *International Journal of Aeroacoustics*, Vol. 20, No. 5-7, 2021, pp. 708–736. https://doi.org/10.1177/1475472X211023831.

[45] Ingard, U., "Influence of Fluid Motion Past a Plane Boundary on Sound Reflection, Absorption, and Transmission," *The Journal of the Acoustical Society of America*, Vol. 31, No. 7, 1959, pp. 1035–1036. https://doi.org/10.1121/1.1907805.

[46] Myers, M., "On the Acoustic Boundary Condition in the Presence of Flow," *Journal of Sound and Vibration*, Vol. 71, No. 3, 1980, pp. 429–434. https://doi.org/10.1016/0022-460X(80)90424-1.

[47] Åbom, M., and Jacob, S., "The Cremer Impedance: Branches, Roots and Low Frequency Damping," *Proceedings of Meetings on Acoustics*, Vol. 39, No. 1, 2019, p. 030002. https://doi.org/10.1121/2.0001426.

[48] "ISO 10534-2:1998, Acoustics — Determination of Sound Absorption Coefficient and Impedance in Impedance Tubes — Part 2: Transfer-function Method," *ISO Standards*, 1998.

[49] COMSOL, "Helmholtz Resonator with Flow: Interaction of Flow and Acoustics," Tech. rep., COMSOL, Application ID: 35011. URL https://www.comsol.com/model/helmholtz-resonator-with-flow-interaction-of-flow-and-acoustics-35011.

[50] d'Elia, M. E., "Flow-acoustic Interaction with Innovative Materials," Ph.D. thesis, Le Mans Université, 2020.